https://doi.org/10.5194/egusphere-2026-4645
Preprint. Discussion started: 1 September 2026

The role of secondary ice production in shaping the microphysical evolution of orographic clouds: A RAMS-ICLAMS modeling study

Ioannis Chaniotis[1,2], Paraskevi Georgakaki[3b], Romanos Foskinis[2,4], Marilena Gidarakou[2,5], Maria Gini[6], Platon Patlakas[1], Konstantinos Eleftheriadis[6], Alexandros Papayannis[2,5], Elissavet Bossioli[1], Nicole Clerx[4], Alexis Berne[4], Helena Flocas[1], and Athanasios Nenes[2,5*]

[1]Division of Environmental Physics and Meteorology, Department of Physics, University of Athens, Athens, Greece
[2]Laboratory of Atmospheric Processes and their Impacts (LAPI), School of Architecture, Civil & Environmental Engineering, Ecole Polytechnique Fédérale de Lausanne, Lausanne, Switzerland
[3]Leipzig Institute for Meteorology, Leipzig University, Leipzig, Germany
[4]Environmental Remote Sensing Laboratory (LTE), School of Architecture, Civil & Environmental Engineering, Ecole Polytechnique Fédérale de Lausanne, Lausanne, Switzerland
[5]Laser Remote Sensing Unit (LRSU), Physics Department, National Technical University of Athens, Zografou, Greece
[6]Environmental Radioactivity & Aerosol technology for atmospheric & Climate impacT Lab (ENRACT), Institute of Nuclear and Radiological Sciences and Technology, Energy and Safety, National Centre of Scientific Research "Demokritos", Ag. Paraskevi, Greece
[b]formerly at: Laboratory of Atmospheric Processes and their Impacts (LAPI), School of Architecture, Civil & Environmental Engineering, Ecole Polytechnique Fédérale de Lausanne, Lausanne, Switzerland

Correspondence to: Athanasios Nenes (athanasios.nenes@epfl.ch)

Abstract. Secondary ice production (SIP) strongly influences ice crystal number concentrations (ICNCs) and cloud microphysical properties, with important implications for radiative forcing, thermodynamics, cloud evolution, and precipitation. Here, we investigate four SIP mechanisms—rime splintering, collisional breakup, rain droplet shattering during freezing, and sublimation breakup—in the Integrated Community Limited Area Modeling System, a specialized version of the Regional Atmospheric Modeling System (RAMS-ICLAMS), during winter storms observed in November–December 2024 as part of the Cleancloud Helmos OrograPhic sIte experimeNt (CHOPIN). Activating SIP increases ICNCs by two to three orders of magnitude and enhances ice water content by up to a factor of 2–3, substantially modifying cloud structure, including a 25–35% reduction in liquid water path and a doubling of ice water path. These changes improve agreement with observed radar signatures and precipitation patterns and alter the amount of precipitation reaching the ground. Among the represented mechanisms, collisional breakup is dominant, followed by rime splintering. Sublimation breakup is locally intense but at least one order of magnitude weaker, while droplet shattering is the weakest and is mainly activated in regions rich in raindrops. The simulated systems encompass synoptic-scale, convective, and stratiform clouds, including snowfall-producing and seeder–feeder configurations. These results highlight the importance of representing SIP—particularly collisional breakup and rime splintering—for realistic simulations of diverse orographic clouds and precipitation in weather- and climate-scale models.

1 Introduction

Mixed-phase clouds play a profound role in the radiation budget and hydrological cycle of the Earth (Vergara et al., 2018; Tan and Storelvmo, 2019) because small changes in the ice–liquid partitioning induce large changes in cloud albedo, lifetime and precipitation efficiency (Mülmenstädt et al., 2015; Heymsfield et al., 2020). Accurately representing the processes governing the generation and evolution of ice in mixed-phase clouds is essential for improving short-term weather forecasts, seasonal predictions and long-term climate projections, and for providing a physically sound assessment of extreme precipitation (Korolev and Field, 2008; Storelvmo, 2017; Georgakaki et al., 2024).

A persistent feature of polar and orographic mixed-phase clouds (especially in the warmer temperatures below -15°C) is that observed ice crystal number concentrations (ICNCs) far exceeds the concentration of measured ice-nucleating particles (INPs) (Korolev and Leisner, 2020, Huang et al., 2022). This implies that primary heterogeneous nucleation of ice cannot alone account for the observed ice abundance (Crosier et al., 2011, Sotiropoulou et al., 2020; Georgakaki et al., 2022) and that secondary ice production (SIP) mechanisms are responsible for this discrepancy. Substantial evidence from laboratory experiments (James et al., 2021; Grzegorczyk et al., 2023), field observations (Korolev et al., 2022), and numerical simulations (Qu et al., 2020; Sotiropoulou et al., 2021; Georgakaki et al., 2024; Grzegorczyk et al., 2025a,b) indicates that the enhancement of ICNCs can be attribured to a range of SIP mechanisms.

Although SIP has been studied for over five decades (Field et al., 2017), yet no single mechanism reproduces the full diversity of observed ICNCs across cloud regimes. The rime-splintering (or Hallett-Mossop) mechanism describes the process upon which small ice splinters are ejected from supercooled droplets that are rimed on the surface of larger ice particles (Hallett and Mossop, 1974). Laboratory studies have shown that this process is effective only within a narrow temperature window (approximately −8 to −3°C) and under specific droplet-size/riming conditions (Hallet and Mossop, 1974, Heymsfield and Mossop, 1984). As such, Hallett-Mossop (HM) alone cannot explain the explosive ICNC observed at temperatures as low as -27°C (Korolev et al., 2022). Collisional breakup (CBR) refers to the mechanical fracturing of fragile ice particles during ice–ice collisions, operating over a much wider temperature range, with peak efficiency near −15 °C (Takahashi et al., 1995, Phillips et al., 2017). Physically motivated parameterizations have been developed to predict the number of fragments generated per collision. The most notable approaches are the temperature-scaling laws derived from laboratory experiments (Takahashi et al., 1995), as well as the calculation of collision kinetic energy (CKE) of various ice hydrometeors (Phillips et al., 2017). This formulation considers the sizes, terminal velocities and rimed masses of each hydrometeor pair, for the calculation of secondary ice fragments. Droplet-shattering (DS) occurs when large rain droplets interact with ice particles. Upon contact, the raindrops begin to freeze from the surface towards the center, resulting in intense pressure build-up and shattering, followed by the creation of many ice fragments (Phillips et al., 2018). Another potentially important process is the sublimation breakup (SUBBR) of large ice particles such as snow dendrites and graupel (Deshmukh et al., 2022). This mechanism is particularly effective in convective or subsaturated environments where rapid sublimation can occur.

https://doi.org/10.5194/egusphere-2026-4645
Preprint. Discussion started: 1 September 2026

In recent years, several studies have incorporated parameterizations for SIP into cloud-resolving, mesoscale, and global models, aiming to better represent observed ICNCs that frequently exceed available INP concentrations. SIP parameterizations have been implemented across a range of modeling systems, including the Weather Research and Forecasting (WRF) model (Sotiropoulou et al., 2020, 2021; Georgakaki et al., 2022, 2024), the Mesoscale Non-Hydrostatic model (Meso-NH) (Hoarau et al., 2018), the Hebrew University Cloud Model (HUCM) (Phillips et al., 2017), the Community Atmosphere Model (CAM6) (Zhao et al., 2021), the Global Environmental Multiscale (GEM) model (Qu et al., 2025), the Icosahedral Nonhydrostatic (ICON) model (Waman et al., 2026), and the DEtailed SCAvenging and Microphysics (DESCAM) 3D bin microphysics scheme (Grzegorczyk et al. 2025). CBR has been included in all such modeling studies to date, reflecting its role as the most predominant SIP mechanism. DS has additionally been implemented by Georgakaki et al. (2022, 2024), Zhao et al. (2021), Qu et al. (2025), Grzegorczyk et al. (2025) and Waman et al. (2026), while sublimation breakup (SUBBR) has been incorporated by Georgakaki et al. (2024) and Waman et al. (2026). SUBBR has been shown to be particularly effective in regions subsaturated with respect to ice, and populated by heavily rimed hydrometeors, complementing the more ubiquitous influence of CBR. In general, these studies show that the inclusion of SIP processes in mesoscale and climate models leads to increases in ICNCs by 2-3 orders of magnitude, with consequential impacts on ice water content (IWC) path (IWP) (Georgakaki et al., 2024), radar reflectivity profiles (Grzegorczyk et al. 2025) and precipitation (Grzegorczyk et al. 2025a,b; Calderón et al., 2025; Floka et al., 2026). Beyond cloud-scale applications, Floka et al. (2026) investigated the impacts of SIP processes on the evolution of the Mediterranean tropical-like cyclone Qendressa (2014), demonstrating improved cyclone track prediction and more realistic precipitation patterns, particularly in regions experiencing extreme precipitation. Within this body of work, Georgakaki et al. (2024) further coupled SIP parameterizations with improved representations of primary INPs, demonstrating substantial improvements in simulated ICNCs and yielding more realistic liquid–ice partitioning and radar signatures that better match observations.

Collectively, these findings highlight the critical role of SIP processes in reproducing observed cloud structures and precipitation enhancement mechanisms such as seeder–feeder dynamics, particularly in orographic environments (Georgakaki et al., 2022). In this context, the seeder–feeder mechanism refers to a precipitation enhancement process in which ice crystals generated in an upper-level cloud layer (the seeder) fall into a lower-level, liquid-rich orographic cloud (the feeder), where they grow efficiently by riming and aggregation. This mechanism strongly enhances precipitation efficiency and is highly sensitive to ICNCs (Proske et al., 2021; Dedekind et al., 2024; Costa-Surós et al. 2026; Frostenberg et al. 2026), making its realistic representation dependent on accurate treatment of SIP and ice–liquid interactions.

Regarding the impacts of SIP on precipitation, Sun et al. (2025) demonstrated that the inclusion of subgrid-scale ice processes spatially modulates precipitation in tropical deep convective clouds simulated with the Unified Model. Specifically, SIP produces a more localized and compact rainfall pattern near the convective core, while reducing domain-averaged precipitation by approximately 8 %. Consistently, Grzegorczyk et al. (2025b) reported that incorporating SIP decreases total precipitation by 15 % and diminishes the occurrence of intense rainfall events (accumulated precipitation

https://doi.org/10.5194/egusphere-2026-4645
Preprint. Discussion started: 1 September 2026

> 40 mm) by 25 %. Furthermore, using the DESCAM 3D bin microphysics scheme, they found that SIP influences both convective dynamics and precipitation characteristics, reducing cloud-top heights by roughly 1.5 km.

Despite the efforts to date on SIP, there are still many important questions that persist regarding the findings of laboratory and experimental studies. These include the sensitivity of SIP to key microphysical parameters, such as the rimed fraction and the size and shape of the parent hydrometeor (Korolev and Leisner, 2020), as well as the representation of fragment size distributions (Phillips et al., 2018), among others. Furthermore, environmental factors that trigger SIP in the atmosphere, such as wind-driven INP fluxes and updraft structure, can complicate the evaluation and validation of model representations. These open questions underscore the need for further research, particularly as many operational numerical weather prediction and climate models either omit SIP entirely or represent it through simplified parameterizations, potentially leading to systematic underestimation of ICNCs in regimes where SIP plays an important role.

While acknowledging these limitations, this study examines with RAMS-ICLAMS the impact of SIP on mixed-phase clouds during two selected cases from the CHOPIN campaign, with a focus on quantifying changes in ICNCs, radar reflectivity, ice and liquid water contents, and precipitation amounts. The model simulations are rigorously evaluated against in situ and ground-based observations to assess the fidelity of SIP representations. This analysis explores how SIP modifies cloud microphysics and precipitation production across distinct cloud regimes observed during the campaign.

2 Methods

2.1 CHOPIN campaign

The Cleancloud Helmos OrograPhic sIte experimeNt (CHOPIN) was a field campaign funded by the EC Horizon Europe Call "Improved knowledge in cloud-aerosol interaction" (https://www.epfl.ch/labs/lapi/chopin-campaign/) and took place between 01/10/2024 and 04/06/2025 at Mount Helmos, Greece. The primary objectives of CHOPIN was to enhance the current understanding of the processes governing the formation and evolution of mixed-phase clouds, as well as to refine and develop algorithms for ground-based and satellite remote sensing of aerosols, clouds, and their interactions. Meteorological observations were conducted at the Helmos Hellenic Atmospheric Aerosol and Climate Change station, namely (HAC)^2, situated near the summit of Mount Helmos at an elevation of 2314 m above mean sea level (AMSL) (37.984° N, 22.193° E). Complementary aerosol, cloud, and boundary-layer measurements were performed at or near the Achilles Base (1760 m, AMSL), located at the Kalavryta Ski Center (38.007° N, 22.196° E). The Achilles Base was equipped with three meteorological radars, the MXPol X-band precipitation radar (9.41 GHz), the MIRA Ka-band cloud radar (35.2 GHz) and the BASTA W-band radar (94.95 GHz). MXPol and MIRA are pulsed, spectral polarimetric scanning radars, whereas BASTA is a bi-static frequency-modulated continuous wave (FMCW) cloud profiler. All radars provide at least the zeroth and first radar moments, i.e. hydrometeor reflectivity and Doppler velocity, however this study focuses mainly on the former, as changes in the simulated hydrometeor size distributions and number concentrations are directly reflected in the radar signal (Georgakaki et al., 2024), making reflectivity a highly relevant metric. In addition, a HALO wind Doppler lidar

https://doi.org/10.5194/egusphere-2026-4645
Preprint. Discussion started: 1 September 2026

(1.5 μm) operating system provided three-dimensional wind measurements, delivering detailed information on wind speed and direction, along with the NTUA and EPFL/NTUA lidars providing profiles of the aerosol optical properties and Planetary Boundary Layer Height (PBLH) (Papayannis et al., 2026). In-situ cloud microphysical measurements were conducted using the Gerber PVM-100 cloud probe, which measures liquid water content and effective droplet radius of ambient clouds by directing a diode-emitted laser beam along a 40-cm sampling path. The forward scattering produced by cloud droplets passing through the open-air measurement volume was detected and converted to liquid water content. Measurements of cloud condensation nuclei (CCN) were performed using the DMT CCN-100 counter, which determines CCN number concentrations by exposing aerosol particles to controlled supersaturation conditions within a continuous-flow thermal gradient chamber (Roberts and Nenes, 2005). Aerosol particles that activate into droplets were detected and counted, allowing the determination of CCN concentrations as a function of supersaturation. Furthermore, measurements of ice-nucleating particles were obtained with the Portable Ice Nucleation Experiment (PINE), the first fully automated instrument designed for laboratory ice nucleation studies and long-term field observations of INPs across a wide temperature range (Möhler et al., 2021). The instrument operates based on a pumped expansion principle to generate water- and ice-supersaturated conditions for aerosol particles sampled either from laboratory setups or natural environments. During operation, the system performs repeated measurement cycles by sampling aerosol particles into a pre-cooled cloud chamber, activating them as supercooled droplets or ice crystals through controlled expansion of the chamber air, and subsequently refilling the chamber with fresh aerosol for the next cycle. The site was also equipped with radiometers, UAV probes, and the EPFL Helikite platform, further enhancing observational capabilities (Fig. 1).

Figure 1: CHOPIN sampling locations on Mount Helmos. (HAC)² located near the mountain top (left), campaign instruments and probe location "Achilles Base" at the Kalavryta Ski Center (right).

2.2 Model description

The model framework used is the Integrated Community Limited Area Modeling System (RAMS-ICLAMS; Solomos et al., 2011), a specialized version of the Regional Atmospheric Modeling System (RAMS) (Pielke et al., 1992; Cotton et al. 2003; Saleeby and van den Heever, 2013) (version 6.0: http://www.atmet.com/software/rams_soft.shtml and version 6.3.04

https://doi.org/10.5194/egusphere-2026-4645
Preprint. Discussion started: 1 September 2026

https://github.com/RAMSmodel/RAMS) developed in part by the Atmospheric and Weather Forecasting Modeling Group (AMWFG) at the National and Kapodistrian University of Athens (NKUA). RAMS-ICLAMS is a non-hydrostatic mesoscale model in operational use at NKUA and has been applied in research over the last three decades (https://forecast.uoa.gr/en/forecast-maps/high-resolution). It resolves eight hydrometeor types—cloud drizzle and rain (liquid), pristine ice, snow, snow aggregates (solid), and graupel and hail (mixed-phase)—which interact through processes such as riming, aggregation, collection, evaporation, and growth. RAMS-ICLAMS also incorporates algorithms for the production, transport, and removal of mineral dust (8-bin) and sea salt (2-bin) aerosols (Spyrou et al., 2010), as well as their cloud- and ice-nucleating properties (Meyers et al., 1992; Nenes and Seinfeld, 2003; Fountoukis and Nenes, 2005; Field et al., 2006; DeMott et al., 2010; Solomos et al. 2011), although these aerosol processes are not explicitly employed in this study, as CCN and INP distributions are directly constrained by observations (consistent with the approach used by Georgakaki et al., 2024). This approach was adopted to simplify the experimental setup and reduce computational cost, while retaining a physically evolving representation of CCN and INP within the cloud model. The explicit prognostic simulation of dust and sea-salt aerosol populations and their coupling to CCN and INP concentrations is left for future work. Such an approach would allow for a more detailed investigation of how the evolution and distribution of aerosol populations regulate primary ice production (PIP) through ice nucleation, and how changes in the resulting primary ice population may subsequently SIP, which is governed by hydrometeor processes but remains coupled to PIP.

Within this study we extended RAMS-ICLAMS to integrate multiple SIP schemes, including the CBR parameterizations of Phillips et al. (2017), which was further refined by Gautam et al. (2024), the DS parameterization of Phillips et al. (2018), and the SUBBR scheme of Deshmukh et al. (2022). Detailed descriptions of the microphysics scheme and the newly implemented SIP mechanisms are provided in the Supplementary Material Section 1. SIP impacts are evaluated using modeled microphysical and remote-sensing proxies, including vertical ICNC profiles, radar Doppler/spectral signatures, reflectivity statistics, and liquid/ice water path (LWP/IWP), with observational data from the CHOPIN campaign. Simulations are focused on periods of storm outbreaks where mixed-phase clouds frequently occur.

2.3 Model Setup, Constraints and Observational Data Used

Initial and boundary conditions were provided by the ERA5 global atmospheric reanalysis dataset, sourced from the European Centre for Medium-Range Weather Forecasts (ECMWF) (Hersbach et al., 2020), available every hour at a spatial resolution of 0.25°×0.25°. Furthermore, aerosol measurements from the CCN-100 and the PINE instruments were used to constrain and calibrate the background concentrations of CCN and INPs employed in the simulations. Meteorological observations collected at the $(HAC)^2$ observatory were used for model evaluation (see Section 2.6), while reflectivity observations from the MIRA cloud radar were used for comparison with the simulated radar fields derived from the model output using a specialized radar simulator (Section 2.5). The MIRA radar provides measurements at a temporal resolution of 5 s, with a range-bin spacing of approximately 31.18 m. To facilitate a direct comparison with the model output, the radar measurements were temporally resampled to 10-min intervals, corresponding to the model output frequency, and

https://doi.org/10.5194/egusphere-2026-4645
Preprint. Discussion started: 1 September 2026

interpolated onto the model levels. Cloud-top height was estimated consistently from both the radar observations and model output, defined as the altitude at which reflectivity falls below −35 dBZ for four consecutive vertical cells.

The model has been set up with three one-way nested domains using a polar stereographic projection (Fig. 2), with a horizontal resolution of 12, 3, and 1 km, respectively. The parent domain (D1) comprises 180×180 grid points and covers the Balkan Peninsula, while the second domain (D2) includes 202×202 grid points, encompassing most of continental Greece. The innermost domain (D3) consists of 293×293 grid points, focusing on the Peloponnese region, where Mt. Helmos is located. The default terrain-following (σ_z) vertical coordinate system has been applied, with the model level thickness starting from Δz=50 m at the surface with a stretching ratio R=1.04 and Δz_{max}=400 m. A total of 85 vertical levels have been employed, reaching up to 20.7 km. Given the horizontal and vertical resolutions of the three nested domains, the Mellor–Yamada level 2.5 turbulence closure scheme was selected which treats turbulent kinetic energy (TKE) as a prognostic variable. Cumulus convection is parameterized using the Kain–Fritsch (1993) scheme in the outer domain (D1), while convection is explicitly resolved in the inner domains (D2 and D3). Radiative transfer is represented using the Harrington radiation scheme, which accounts for the radiative effects of aerosols and hydrometeors by explicitly calculating their associated optical depths. All simulations were configured using the model two-mode CCN representation (NAMELIST option IAEROSOL=1) and an INP field described by the formulation of DeMott et al. (2010) (NAMELIST option IIFN=2), initialized with exponential vertical profiles that satisfy the mass transfer equations, with no additional sources or sinks except for regeneration and removal by hydrometeors (NAMELIST option IAERODEP=1). This approach was adopted to minimize uncertainties and numerical noise in the case study. Based on the analysis of time series (not shown in this study) of CCN and INPs measured by the DMT CCN-100 (at supersaturation 0.3%) and PINE instruments (at -25°C), all model simulations were configured with CCN number concentration profiles of 600 mg^{-1} (fine mode) and 0.01 mg^{-1} (coarse mode), and an INP profile of 0.003 mg^{-1} at the model surface, assuming an exponential decrease with model height. A summary of the model setup and its main characteristics is presented in Table 1.

Table 1: Configuration of the RAMS-ICLAMS modeling system

Simulation characteristic	Selected parameter/option
Model domains	D1: 180×180 points - Δx=12 km
	D2: 202×202 points - Δx= 3 km
	D3: 293×293 points - Δx=1 km
Vertical level structure	85 levels, Δz_0=50m, Δz_{max}=400m, R=1.04
Integration time – timestep	60h, 15s (D1), 3.75s (D2), 1.25s (D3)
Microphysics scheme	Meyers et al., (1997), Saleeby et al., (2013)
Aerosols – CCN	Fine-Coarse Mode (IAEROSOL=1)
INP parameterization	DeMott et al., (2010)
Cloud droplet activation scheme	Walko et al., (1995), Fountoukis and Nenes, (2005)
Turbulence closure scheme	Mellor-Yamada 2.5, Mellor and Yamada, (1992)
Radiation scheme	Harrington, (1997)

https://doi.org/10.5194/egusphere-2026-4645
Preprint. Discussion started: 1 September 2026

Convective parameterization scheme	Kain and Fritsch; 1993 (only for D1)
Initial & boundary data assimilation	ERA5 Reanalysis (0.25°x0.25°) Hersbach et al., (2020)
Topography	U.S. Geological Survey (1996). GTOPO30: Global 30-Arc-Second Elevation
Vegetation/Land use	MODIS Land Cover 2015-2019 Raster 100m Global
Soil texture	FAO-UNESCO Soil Map of the World (0.5°x 0.5°)

Regarding the implemented SIP mechanisms, the CBR process is activated upon ice-ice collision; RAMS-ICLAMS, however, does not explicitly track the rimed fraction of hydrometeors. Following Georgakaki et al. (2024), a characteristic rimed fraction of $\psi = 0.25$ was prescribed for CBR and this mechanism was limited to hydrometeors with a characteristic size exceeding 100 μm. Pristine ice self-collection was assumed not to produce secondary ice, owing to its small particle size and negligible differential terminal velocity. Activation of CBR in the model requires the presence of liquid hydrometeors (raindrops or cloud droplets) in the same instant (timestep) and location (grid cell) as the ice particles. All secondary ice fragments generated by CBR are assigned to the pristine ice category.

The DS process incorporates two distinct fragmentation modes associated with ice multiplication. The first mode occurs when a supercooled raindrop either collides with a smaller cloud ice particle or freezes through immersion nucleation initiated by an INP. In this mode, two families of ice fragments are generated: small fragments, which are assigned to the pristine ice category, and larger fragments, which, according to Phillips et al. (2018), may span a relatively broad size spectrum. In the present study, however, all large fragments produced through this mechanism are assumed to be transferred to the hail category. The number of fragments generated in this mode depends on the product of the droplet freezing probability and the shattering probability. The freezing probability is set to unity for temperatures below −6°C and to zero above −3°C, with a cubic interpolation applied between these temperature limits. The shattering probability is parameterized as a function of raindrop diameter, with a value of zero for diameters below 50 μm and unity for diameters above 60 μm, with a smooth transition between these limits. The second fragmentation mode occurs when supercooled raindrops collide with larger ice particles, such as snow or graupel. These collisions also produce ice fragments; however, following Georgakaki et al. (2024), all fragments generated through this mechanism are assumed to belong to the pristine ice category. Thus, unlike the first fragmentation mode, no distinction between small and large fragments is made in their subsequent categorization in the present study.

Apart from SIP from hydrometeor collisions, SUBBR has also been included in RAMS-ICLAMS. This process occurs when dendritic or heavily rimed ice particles undergo sublimation under subsaturated conditions within downdrafts, leading to the detachment of branches or other fragile protrusions. In RAMS-ICLAMS, SUBBR is restricted to temperatures between −10 °C and −20 °C, a range that aligns with the preferential growth habit of dendritic snow particles. More details can be found in Supplementary Material S1.4.

https://doi.org/10.5194/egusphere-2026-4645
Preprint. Discussion started: 1 September 2026

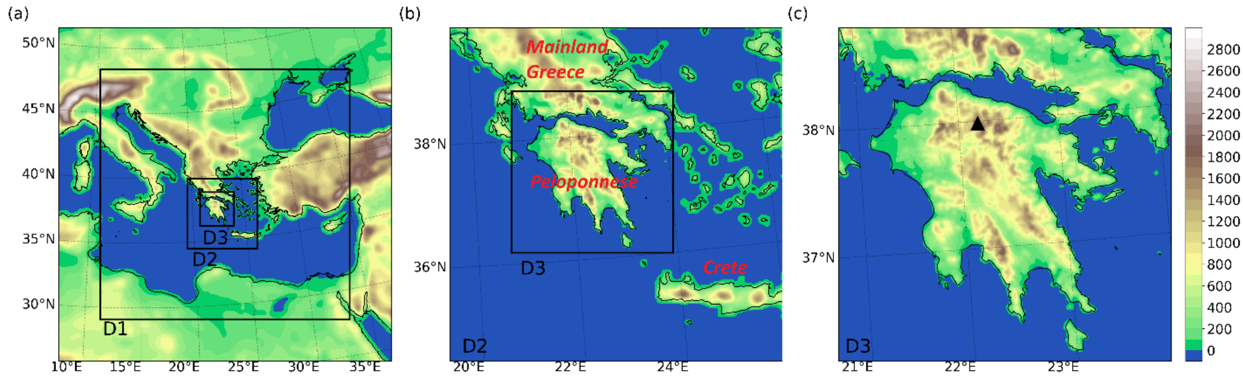

Figure 2: Model domains D1, D2 and D3 over southeastern Europe (a), central-south mainland Greece-D2 (b) and the Peloponnese-D3. Color contours indicate terrain heights in meters. The experimental site is indicated by the black triangle.

2.4 Case studies & sensitivity simulations

During the CHOPIN campaign, two meteorologically active periods were selected to investigate cloud and precipitation processes under conditions favorable for ice formation and SIP. The first case (namely Convective Cloud Case: CC) spans from 11 November 2024 at 00 UTC to 13 November 2024 at 00 UTC, and the second case (namely Stratiform Cloud Case: SC) from 6 December 2024 at 00 UTC to 8 December 2024 at 00 UTC. Both cases are characterized by ice-rich cloud systems driven by a combination of large-scale forcing and orographic lifting, but they represent distinct cloud regimes commonly observed over the region.

CC is dominated by a mature mid-tropospheric cut-off low centered at approximately 500 hPa over the Balkans (Fig. S1a), with temperatures in the low core reaching about −33°C. The nearly symmetric geopotential height and temperature fields indicate strong thermodynamic instability and sustained upward motion, and predominant convective cloud structures (Galani et al., 2003). The Peloponnese lies south of the low center, where westerly flow advects moist air masses into the region, supporting deep convective cloud development with cloud tops reaching up to ~10 km above ground level ( ) and producing significant precipitation. In contrast, SC features a well-defined mid-tropospheric trough over the central-western Balkans (Fig. S1b), with minimum temperatures of approximately −27°C along the trough axis. This configuration induces strong northwesterly flow upstream and southwesterly flow downstream of the trough, enhancing moisture transport and orographic uplift over southern Greece. Residual influences from a prior disturbance south of Crete further modulate the thermodynamic environment, favoring the formation of shallower (up to 6 km AGL), predominantly stratiform orographic clouds that nevertheless produce substantial precipitation.

For each case, two simulations were performed to isolate the effects of SIP on cloud and precipitation evolution: one including the newly implemented SIP mechanisms – HM, CBR, DS, and SUBBR - and one excluding these processes. Simulations with SIP enabled are referred to as ALLSIP, while those without SIP are denoted as CONTROL. Although the original RAMS-ICLAMS code incorporates HM, this mechanism is deactivated for the CONTROL simulations.

https://doi.org/10.5194/egusphere-2026-4645
Preprint. Discussion started: 1 September 2026

2.5 The CR-SIM Forward Radar Simulator

To evaluate the model simulations and gain insight into the cloud microphysical processes over the region of interest, the Cloud Resolving Model Radar Simulator (CR-SIM, version 4.0) (Oue et al., 2020) was coupled to the output of the RAMS-ICLAMS simulations. CR-SIM is a forward-modeling operator that emulates ground-based radar and lidar observables from high-resolution cloud-resolving model output, enabling direct and consistent comparisons between simulated atmospheric fields and remote-sensing measurements. The simulator combines microphysical model variables with pre-computed electromagnetic scattering properties to generate synthetic radar observables, including reflectivity, Doppler velocity, spectral width, and polarimetric variables, as well as lidar backscatter and extinction profiles. Synthetic measurements are produced separately for each hydrometeor category, accounting for their particle size distributions and dielectric properties. The scattering characteristics of both frozen and liquid hydrometeors are calculated using the T-matrix method and stored in look-up tables that are subsequently used to derive radar observables. The simulator has been extensively utilized in recent studies (Vignon et al., 2019; Vignon et al., 2021; Georgakaki et al., 2024) to study the importance of SIP mechanisms and their predicted signature in the cloud radar spectra.

In this study, CR-SIM was driven by the outputs from the CONTROL and ALLSIP simulations (representing convective and stratiform conditions) performed with RAMS-ICLAMS. The simulator was configured to reproduce the observational characteristics of the in-situ cloud radar MIRA cloud radar located at the Achilles Base (Fig. 1). The simulated radar operated at a frequency of 35.4 GHz, corresponding closely to the Ka-band frequency of the instrument. The radar elevation angle was set to 90°, representing a vertically pointing configuration. Although the MIRA radar operated in scanning mode during several observational periods, only measurements acquired when the radar was pointing vertically were used in the analysis to ensure consistency with the simulator setup. The radar beamwidth was set to 0.5°, matching roughly the characteristics of the deployed instrument. In addition, the field of view of the collocated Microwave Radiometer was represented with a 0.53° viewing angle. CR-SIM calculations were performed using the model grid cell located closest to the Achilles Base. The resulting synthetic radar variables—corrected for total hydrometeor attenuation—were produced at each vertical model grid level, facilitating direct comparisons with the corresponding radar observations.

2.6 Model Evaluation

Model evaluation was performed for the CC and SC CONTROL experiments using meteorological observations from the (HAC)[2] weather station, including basic meteorological variables such as the near surface temperature and relative humidity, as well as wind speed and wind direction (retrieved at approximately 10m AGL) (Fig. S2). Model outputs extracted from the nearest grid point and interpolated to the corresponding level are compared against the observed values. For both periods, the model was initialized at 12:00 UTC on the preceding day and integrated for a 12-hour spin-up period. The spin-up period was excluded from the analysis, and the results presented in the manuscript correspond only to the aforementioned examined periods.

https://doi.org/10.5194/egusphere-2026-4645
Preprint. Discussion started: 1 September 2026

In CC, the observed temperature shows a very small variation from 0 to 4°C which is also captured well by the modeled values (Fig. S2a). The root mean square error (RMSE) for temperature is $RMSE_T$=0.91°C. Relative humidity ranges at 80-100%, however the model predicts drier conditions during the 12/11 00-08 UTC, with $RMSE_{RH}$=15.65%. In SC both temperature (T) and relative humidity (RH) are well represented by RAMS-ICLAMS, with $RMSE_T$=1.29°C and $RMSE_{RH}$=6.15%. Temperature spans between -4 to +1°C and relative humidity remains at 90-100%, indicating conditions close to saturation (Fig. S2c). Wind speed poses significant variation in both cases. In CC, the 5min average value rises from 5ms^{-1} at 2024-11-11 06 UTC to 15ms^{-1} at 2024-11-12 18 UTC, however there is a significant variance of up to 15ms^{-1} between 2024-11-12 10 UTC and 18 UTC, indicating turbulent conditions. The wind direction changes rapidly from 280° (W) to ~150° (SE) at 2024-11-11 06 UTC, which is attributed to the passage of a frontal system (Fig. S2b). The modelled wind speed captures the overall temporal evolution well, although it exhibits a systematic underestimation of up to 2 ms^{-1}. The resulting RMSE for wind speed at 10 m AGL is $RMSE_{WS}$=3.25 ms^{-1}. The transition of the modelled wind vector is also smoother compared to observations, an expected behavior given the complex topography of the region and the model's inherent spatial smoothing.

A similar pattern is found in SC. The observed wind speed gradually decreases from 10 ms^{-1} at 2024-12-06 00 UTC to 4 ms^{-1} at 2024-12-06 20 UTC, followed by an increase to 17 ms^{-1} by 2024-12-08 00 UTC. The period from 2024-12-07 06–16 UTC is marked by strong fluctuations (Fig. S2d). Wind direction also shifts slowly from 100° (ESE) to 230° (SW). The model successfully reproduces these general trends in both wind speed and direction, although it overpredicts wind speed by about 7 ms^{-1} at 2024-11-07 12 UTC, with $RMSE_{WS}$=3.61 ms^{-1}. Despite these discrepancies, mainly induced by the site's complex terrain, the model demonstrates overall robust behavior, reliably capturing the key features of the observed wind field.

3 Results and discussion

In the following section, each case study (CC & SC) is presented individually following a consistent framework. The analysis begins with the evaluation of changes in the vertical evolution of ICNC profiles between the CONTROL and ALLSIP simulations, followed by an assessment of the corresponding modifications in radar reflectivity. Subsequently, time–height distributions of IWC and LWC are compared, together with time series of an area-averaged IWP and LWP. The next subsections address the contribution of individual SIP mechanisms, highlighting the spatial and temporal domains where each mechanism predominates, and summarizing their overall contributions using pie charts. The final subsection concludes with an examination of the temporal evolution of accumulated precipitation.

3.1 Comparison of ICNC evolution: Convective Case (CC)

Figure 3 illustrates the temporal evolution of the vertical profiles of ICNC, defined as the sum of all solid hydrometeor number concentrations ($N_{ice} + N_{snow} + N_{aggregates} + N_{graupel} + N_{hail}$), presented on a logarithmic scale spanning 10^{-2} (dark blue) to 10^4 L^{-1} (yellow), for CC. Superimposed are the vertical temperature fields (black dashed and solid contours) and the mean

https://doi.org/10.5194/egusphere-2026-4645
Preprint. Discussion started: 1 September 2026

hydrometeor aggregation rates over selected time intervals (colored curves). Temperature ranges from +6°C near the surface to -55°C at the cloud top. Both the CONTROL and ALLSIP experiments exhibit pronounced cloud development during the second 24-hour period (12–13 November), with cloud layers extending from the surface to approximately 10 km. Most of the cloud mass resides above the freezing level (solid black line) and is characterized by elevated ice crystal number concentrations on the order of 1-1000 L^{-1}. The most substantial differences between CONTROL and ALLSIP occur within the lower cloud layers, where SIP processes are taking place (Fig. 6) and liquid water is also available for riming with ice particles (Fig. S3). In ALLSIP, ICNC increases by up to two orders of magnitude from the surface to ~5 km, accompanied by an expansion of regions with enhanced hydrometeor aggregation. These enhancements are particularly evident on 12 November between 08–14 UTC and 18–23 UTC and are conducive to intensified hydrometeor growth and subsequent precipitation formation, consistent with previous studies (Sotiropoulou et al., 2021; Georgakaki et al., 2022). The temperature field remains largely unchanged between the two simulations, while a modest reduction in ICNC is detected in the upper cloud layers.

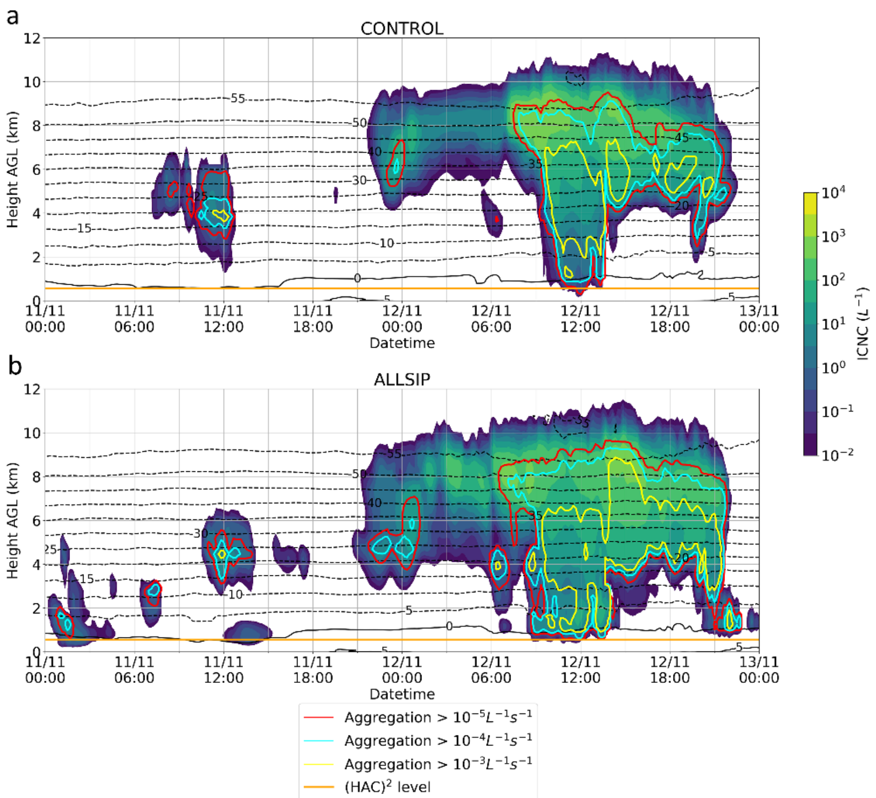

Figure 3: Simulated ICNC (L^{-1}) from the a) CONTROL and b) ALLSIP experiments for CC, with red, cyan, and yellow contours depicting different aggregation rate levels (L^{-1} s^{-1}). Black dashed contours indicate temperature in 5 °C intervals, and the solid orange line marks the height of the (HAC)² station. This time–height cross section is centered over the Achilles Base.

https://doi.org/10.5194/egusphere-2026-4645
Preprint. Discussion started: 1 September 2026

The temporal evolution of the relative contributions of the different ice hydrometeor populations is shown in Figure S4. In CONTROL, pristine ice dominates the ICNC during the main convective period, with snow and aggregates contributing substantially at later times, while the total ICNC peaks at around 80 L^{-1}. In ALLSIP, the ice population is generally more variable and includes larger contributions from snow, aggregates, and graupel, with pristine ice still dominant during much of the active period. The ALLSIP simulation reaches a slightly higher peak ICNC (about 80–85 L^{-1}) and exhibits stronger temporal variability and over higher values, except from the period 12/11 06-12 UTC, indicating that the treatment of SIP substantially modifies both the magnitude and composition of the ice hydrometeor population.

3.2 Comparison of radar signatures: Convective Case (CC)

Figure 4 displays the temporal evolution of reflectivity (dBZ) profiles for (a) CONTROL, (b) ALLSIP, and (c) MIRA measurements for CC. During the first 24 hours, observed reflectivity ranges from −30 to +20dBZ below 4 km (Fig. 4c), but this shallow cloud structure is not well captured by either CONTROL or ALLSIP. The second 24-hour period is more informative, as clouds become more vertically developed, with reflectivity reaching up to 38 dBZ on 12 November between 10–14 UTC and 18–21 UTC, extending from the surface to about 6 km AGL. Both CONTROL (Fig. 4a) and ALLSIP (Fig. 4b) reproduce this structure more accurately. Nevertheless, a qualitative comparison indicates that reflectivity is generally overestimated in the main cloud volume, with a more pronounced overestimation in regions of enhanced sedimentation, signified by high reflectivity values below 1.5 km, at 12/11 09-15 UTC and 19-21 UTC.

To quantify these differences, time-averaged and maximum reflectivity profiles were calculated over the Achilles Base for the period 12 November 06 UTC to 13 November 00 UTC (Fig. S5a), selected because of the elevated reflectivity values especially below 1-1.5 km AGL, indicating notable sedimentation during this period (Fig. 4). The time-averaged MIRA profile exhibits a gradual decrease in reflectivity with height, from approximately 10 dBZ within the lowest 1 km AGL to around 0 dBZ between 3 and 5 km AGL, and below −15 dBZ at 8–9 km AGL. CONTROL substantially underestimates the observed mean reflectivity in the lowest 3 km AGL, with differences of approximately 5–10 dBZ, while overestimating reflectivity aloft by approximately 3–10 dBZ. In contrast, ALLSIP produces systematically higher mean reflectivity values throughout most of the cloud profile and is, on average, approximately 2 dBZ higher than CONTROL, with a local difference of up to approximately 5 dBZ near 1.5 km AGL. This enhancement occurs in a temperature range of approximately −5 to −10°C, where the full set of SIP mechanisms is active, suggesting that the enhanced reflectivity in ALLSIP is linked to the activation of SIP-related microphysical processes and their impact on the simulated hydrometeor population. Apart from the time-averaged values, the maximum reflectivity profiles provide additional insight into the strongest observed and simulated hydrometeor signatures. Both CONTROL and ALLSIP consistently exhibit higher maximum reflectivity than MIRA within the lowest approximately 6 km AGL, with differences generally ranging from 3 to 6 dBZ. ALLSIP further increases the maximum reflectivity relative to CONTROL by approximately 0–5 dBZ over this layer, with an average difference of approximately 1.8 dBZ. These results indicate that, while the inclusion of SIP processes

https://doi.org/10.5194/egusphere-2026-4645
Preprint. Discussion started: 1 September 2026

improves the overall representation of the observed reflectivity structure and sedimentation-related variability, it also tends to enhance the strongest reflectivity signatures beyond those observed by MIRA.

The statistical evaluation of the time-averaged reflectivity profiles further supports these findings. The mean bias is reduced substantially from −3.11 dBZ in CONTROL to −0.34 dBZ in ALLSIP, indicating a considerable improvement in the overall agreement with observations following the inclusion of SIP processes. The corresponding MAE decreases from 7.09 to 6.31 dBZ, while the RMSE decreases from 7.80 to 7.35 dBZ. Thus, although the improvement in the overall error metrics is moderate, the strong reduction in mean bias suggests that ALLSIP provides a more balanced representation of the vertical reflectivity distribution. Overall, these results suggest that the activation of SIP processes improves the representation of the cloud's vertical reflectivity structure and sedimentation-related features, while also introducing a tendency toward enhanced reflectivity. Regarding the cloud tops, observations indicate a steady fluctuation between 3.5-5km during the first 24h and a sharp transition to 8-8.5 km during the development of the convective clouds, during the last 24h. Although, the structure exhibits discontinuity, with cloud gaps between 12 November 00 and 10 UTC. Both CONTROL and ALLSIP simulations overestimate the cloud tops by up to 1 km and predict a more compact cloud structure.

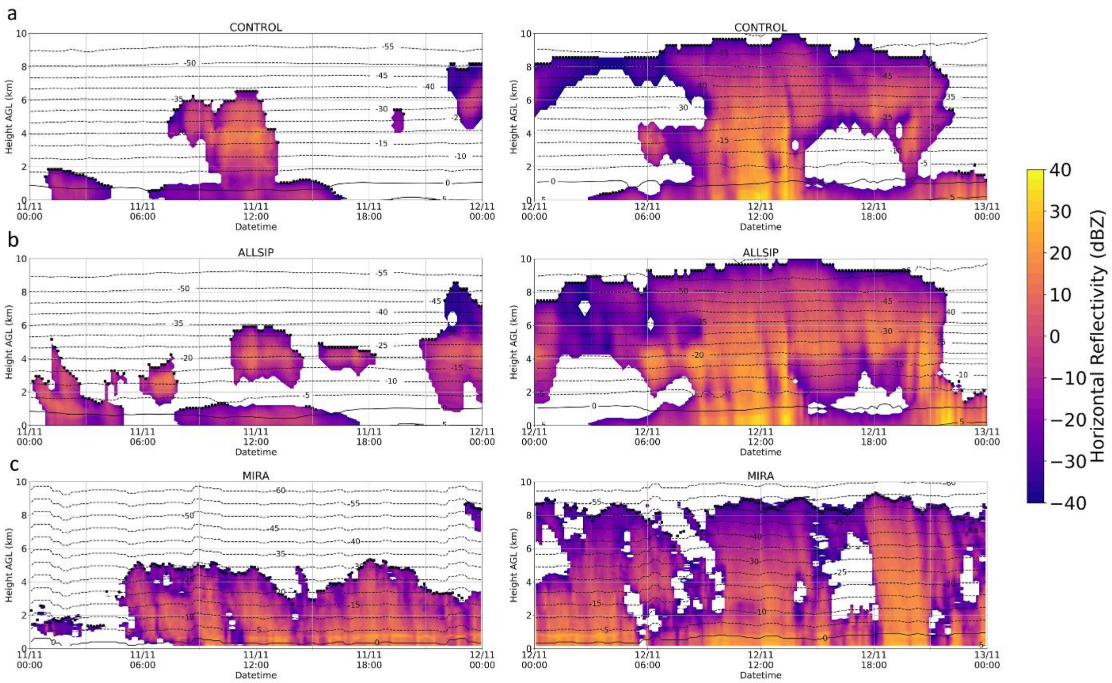

Figure 4: Simulated radar reflectivity (dBz) from CR-SIM, generated using RAMS outputs for the CONTROL (a) and ALLSIP (b) experiments, alongside MIRA in-situ reflectivity observations (c). Black dashed contours in (a) and (b) represent temperature in 5 °C intervals. Black squares indicate cloud-top height. Time–height cross section is centered over the Achilles Base.

https://doi.org/10.5194/egusphere-2026-4645
Preprint. Discussion started: 1 September 2026

3.3 Spatiotemporal distribution of IWC and LWC - Comparison of IWP and LWP: Convective Case (CC)

The spatiotemporal evolution of IWC and LWC is shown in Fig. S3. In the CONTROL run, the main hydrometeor development occurs on 12 November, when a vertically developed cloud structure forms. IWC remains relatively modest, with peak values reaching approximately 0.6 gm^{-3} (November 12, 10-14 UTC), primarily concentrated within the lower mixed-phase region between ~0.5 and 1.5 km AGL. Above this level, ice particles extend intermittently up to ~8–9 km AGL, although the associated IWC values remain below 0.2 gm^{-3} (Fig. S3a). The corresponding LWC field indicates a shallow liquid layer confined mostly below ~1.7 km AGL, with maximum values of about 0.8–1.0 gm^{-3} occurring near 1–1.5 km AGL around 12 November, 06-18 UTC (Fig. S3c).

The ALLSIP simulation exhibits substantially enhanced IWC and a more vertically coherent cloud structure. Maximum IWC increases to approximately 0.9–1.0 gm^{-3}, nearly doubling the peak values obtained in the CONTROL run. These maxima occur at similar times but are centered slightly higher, around ~0.8–1.2 km AGL. Ice particles are distributed more continuously throughout the column, extending from the lower mixed-phase region to ~8–9 km AGL, indicating a more persistent and vertically developed ice phase (Fig. S3b). The liquid phase is not significantly changed in ALLSIP, with peak LWC values reaching ~0.9 gm^{-3}; a small reduction is present around November 12, 12-20 UTC.

Overall, the most pronounced differences between the simulations occur within the ~0.8–2 km AGL layer, corresponding to the mixed-phase temperature regime, where ALLSIP produces higher IWC relative to CONTROL. This results in a thicker and more persistent mixed-phase cloud layer and a more continuous vertical distribution of ice, suggesting that the ALLSIP configuration substantially strengthens cloud microphysical development compared to the baseline simulation.

Figure S6 presents the time series of IWP and LWP. The IWP represents the vertical integral of the mass concentration of all ice-phase hydrometeors (cloud ice, snow, aggregates, graupel, and hail), while the LWP corresponds to the vertical integral of all liquid-phase hydrometeors (cloud droplets, drizzle, and rain). These quantities are also averaged in a 5×5 km^2 region around Achilles base (Fig. 1) to reduce the impact of spatial shifts of the cloud structure. During CC, a substantial amount of IWP is present between 2024-11-12 06 UTC and 2024-11-13 00 UTC (Fig. S6a), with three distinct peaks occurring near 12, 14 and 22 UTC on 12 November.

Overall, the ALLSIP simulation consistently produces higher IWP values than the CONTROL run. The first peak reaches 1.35 gm^{-2} in ALLSIP compared to 1.32 gm^{-2} in CONTROL, while the second peak is 2.67 gm^{-2} in ALLSIP versus 1.49 gm^{-2} in CONTROL, and stays consistently higher during the next hours. On average, the IWP increases by about 35% in the ALLSIP scenario, highlighting the influence of SIP processes. During the same period, the LWP exhibits two pronounced peaks on November 12, 14 and 22 UTC, varying between 0 and 1.32 gm^{-2} (Fig. S6b). The differences between the CONTROL and ALLSIP simulations are small, with the ALLSIP run showing an average decrease of about 10% during the first peak, and a follow-up decrease of approximately 10% in the second peak. Furthermore, there is an average reduction of ~5% for the whole experiment. This slight reduction is expected, as liquid water is depleted through enhanced ice growth

https://doi.org/10.5194/egusphere-2026-4645
Preprint. Discussion started: 1 September 2026

processes, such as collection, contact freezing, and riming, associated with the increased ice hydrometeors in the ALLSIP simulation.

The analysis continues by focusing on $(HAC)^2$, where the in-situ measurements of LWC derived from the PVM-100 probe are available (Fig. 5). Observations show generally low LWC values during the first part of the period, followed by an increase from approximately 0.1–0.2 gm^{-3} on 11 November to 0.2–0.3 gm^{-3} on 12 November, with substantial short-term variability and occasional peaks reaching ~0.5 gm^{-3}. Toward the end of the period, observed LWC remains highly variable, with values generally around 0.1–0.3 gm^{-3} and brief peaks of up to ~0.5 gm^{-3}. CONTROL exhibits a similar overall temporal evolution but tends to produce higher LWC values, particularly during the later part of 12 November, when values frequently reach ~0.4–0.5 gm^{-3} and peak at approximately 0.8 gm^{-3}. In contrast, ALLSIP generally predicts lower LWC, with values mostly around 0.2–0.4 gm^{-3} during the main cloud period and occasional peaks of ~0.6–0.7 gm^{-3}. Thus, despite discrepancies between both simulations and the observations, ALLSIP generally yields lower LWC values and is, overall, somewhat closer to the PVM-100 observations than CONTROL.

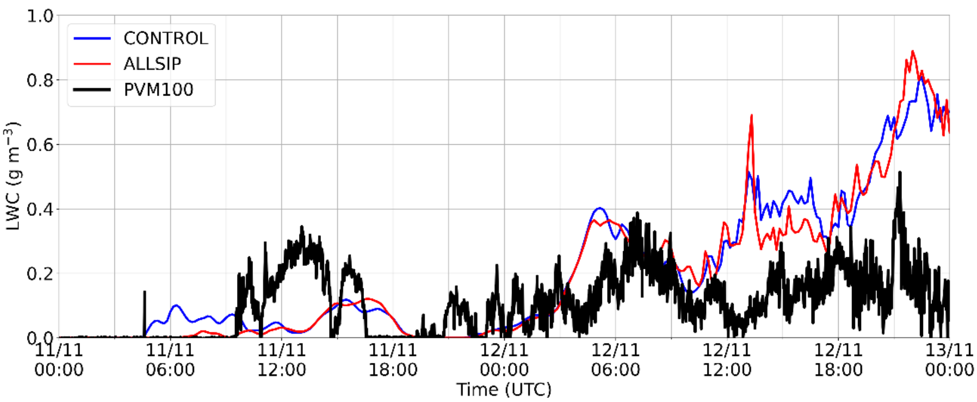

Figure 5: Timeseries of LWC for the convective case (CC). The blue line represents the CONTROL, the red line the ALLSIP simulations and the black line observations at (HAC)2 with the PVM-100 instrument.

3.4 Comparison of SIP rates and precipitation: Convective Case (CC)

The spatial variability of ICNC can be interpreted by identifying where the different SIP mechanisms are activated within the cloud. Figure 6 presents the temporal evolution of ICNC together with the SIP rates associated with the four SIP processes, CBR, HM, DRS, and SUBBR, for CC. Among the mechanisms, CBR emerges as the most efficient, with production rates typically ranging from 10^{-4} to 10^{-2} L^{-1} (purple contours). CBR activation is most pronounced within the lower cloud layers at temperatures between -25°C and -5°C, consistent with established theoretical and observational studies by Phillips et al. (2017) and Korolev et al. (2022). CBR exhibits a distinct maximum on 12 November 2024 between 12–23 UTC, with rates reaching 10^{-3}-10^{-2} L^{-1}. The second most influential mechanism is HM (red contour) also exhibiting production rates of 10^{-4}-10^{-2} L^{-1} but in a narrow region, about 1.5km AGL, where temperature ranges in -8 to -3°C. SUBBR (magenta contours) is the

https://doi.org/10.5194/egusphere-2026-4645
Preprint. Discussion started: 1 September 2026

third strongest, which is restricted primarily to the -20 to -10°C layer within the lowest ~4 km of the atmosphere and is associated with regions of low ice supersaturation (not shown), in accordance with the Deshmukh et al. (2022) parameterization. Mean SUBBR production rates are on the order of 10^{-4} L^{-1}. The DS mechanism plays a comparatively smaller role in this study. It is activated within the lowest ~2 km of the cloud at temperatures between -10°C and 3°C (cyan contours). In this case (CC), DS is characterized by isolated hotspots. Average production rates range from 10^{-6} to 10^{-5} L^{-1}. Overall, the spatial and temporal correspondence between regions of active SIP and elevated ICNC is evident, although transport and precipitation processes also influence the resulting ICNC distributions.

Regarding accumulated precipitation at the site, as shown in Fig. S7, the value increases substantially during the last 12 hours of the experiment (2024-11-12 12 UTC to 2024-11-13 00 UTC), reaching a maximum of 8.7 mm in the CONTROL run. In contrast, the ALLSIP scenario produces consistently higher precipitation, reaching 13.8 mm (+58.6%).

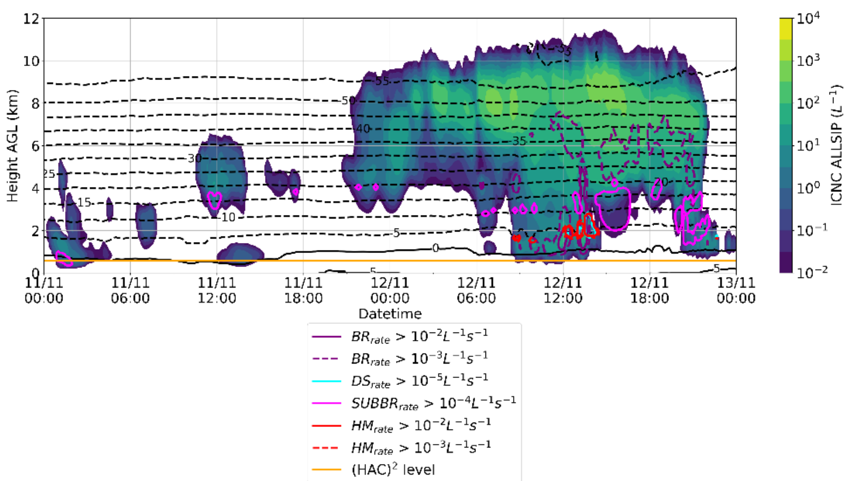

Figure 6: Simulated ICNC (L^{-1}) and SIP production rates from the CC ALLSIP experiments. Solid purple contours indicate areas where $BR_{rate}>10^{-2}$ $L^{-1}s^{-1}$, solid red contours indicate areas where $HM_{rate}>10^{-2}$ $L^{-1}s^{-1}$, dashed red contours areas where $HM_{rate}>10^{-3}$ $L^{-1}s^{-1}$, solid cyan contours areas where $DS_{rate}>10^{-5}$ $L^{-1}s^{-1}$, and solid pink contours areas where $SUBBR_{rate}>10^{-4}$ $L^{-1}s^{-1}$. Black dashed contours indicate temperature in 5°C intervals, and the solid orange line marks the height of the (HAC)² station. This time–height cross section is centered over the Achilles Base.

Beyond the spatiotemporal evolution of SIP, we quantify the relative contribution of the individual SIP mechanisms (Fig. 7a). Percentages were calculated by integrating the contribution of each interaction pair within a 5×5 km² area centered on Achilles Base and vertically summing from the surface to the model top. CBR processes are grouped into five categories according to the interacting hydrometeor types: (i) graupel/hail–graupel/hail, (ii) snow/aggregate–graupel/hail, (iii) pristine cloud ice–graupel/hail, (iv) cloud ice–snow/aggregate, and (v) snow/aggregate–snow/aggregate. The two modes of droplet shattering (DS) are combined into a single category.

CBR dominates the total SIP budget, accounting for 72% of the ice particles produced secondarily. Within this category, the largest contributions arise from snow/aggregate–graupel/hail collisions (~26%), followed by snow/aggregate–

https://doi.org/10.5194/egusphere-2026-4645
Preprint. Discussion started: 1 September 2026

snow/aggregate collisions (~22%) and cloud ice–snow/aggregate interactions (~19%). Collisions between cloud ice and graupel/hail contribute approximately 6–7%, while interactions involving the largest hydrometeors (graupel or hail) account for only ~4%, with graupel/hail–graupel/hail collisions contributing <2%. The HM mechanism represents the second most important source of secondary ice, contributing approximately 24% of the total SIP. In contrast, SUBBR contributes about 4%, while DS provides a negligible contribution (<1%). Overall, the partitioning of SIP mechanisms is broadly consistent with previous studies, including Phillips et al. (2017b) and Grzegorczyk et al. (2025), despite differences in cloud dynamics among the simulations. Nevertheless, the relative importance of these processes is expected to vary under different environmental conditions, particularly in environments characterized by warmer temperatures, stronger updrafts, and enhanced supercooled liquid water content.

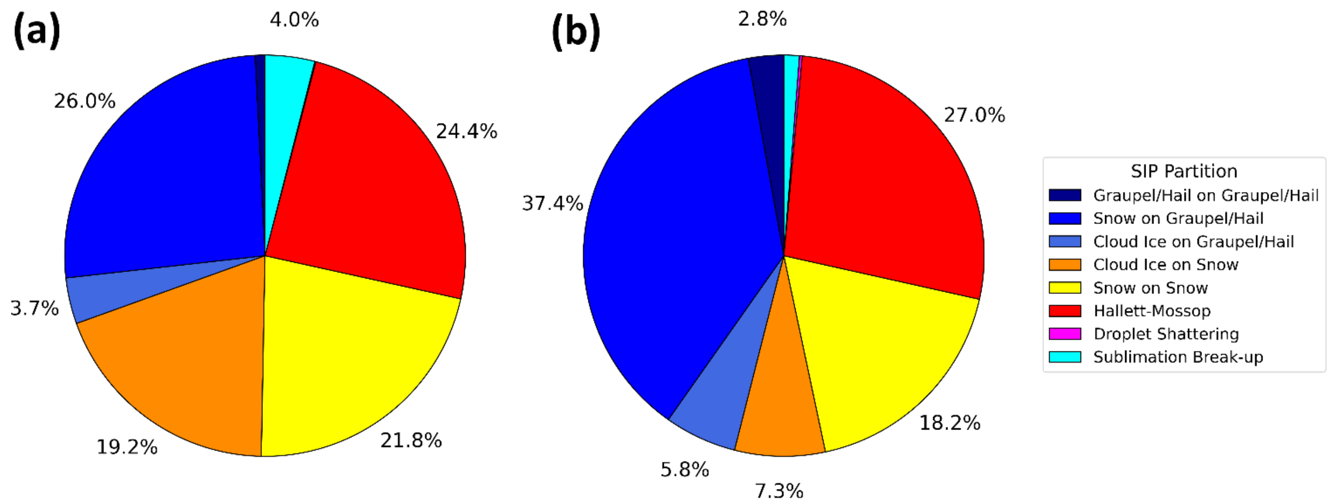

Figure 7: Total contribution by SIP mechanism for (a) CC and (b) SC. CBR mechanisms (dark blue hues/yellow/orange), HM (red), DS (cyan), and SUBBR (magenta). Percentage labels shown only for contributions > 2%.

3.5 Comparison of ICNC evolution: Stratiform Case (SC)

Figure 8 illustrates the temporal evolution of the vertical profiles of ICNC, the vertical temperature fields, and the mean hydrometeor aggregation rates over selected time intervals. Temperature ranges from +5°C near the surface to -55°C at the cloud top. During the first 24-hour period, a compact cloud layer is evident between 4 and 9 km, exhibiting ice crystal number concentrations of 10-1000 L^{-1} (Fig. 8a). Additional cloud structures also appear at lower altitudes between 00–03 UTC and 12–18 UTC. During the second 24-hour period, the cloud field becomes temporally intermittent and shifts to lower levels, extending from the surface to approximately 6 km. Nevertheless, high ice crystal concentrations of 100-1000 L^{-1} persist within these layers. In the ALLSIP experiment (Fig. 8b), ICNC again increases by up to two orders of magnitude,

https://doi.org/10.5194/egusphere-2026-4645
Preprint. Discussion started: 1 September 2026

primarily within the lower troposphere (up to ~4 km), while a slight reduction is noted at higher altitudes. Correspondingly, hydrometeor aggregation rates are enhanced within these regions.

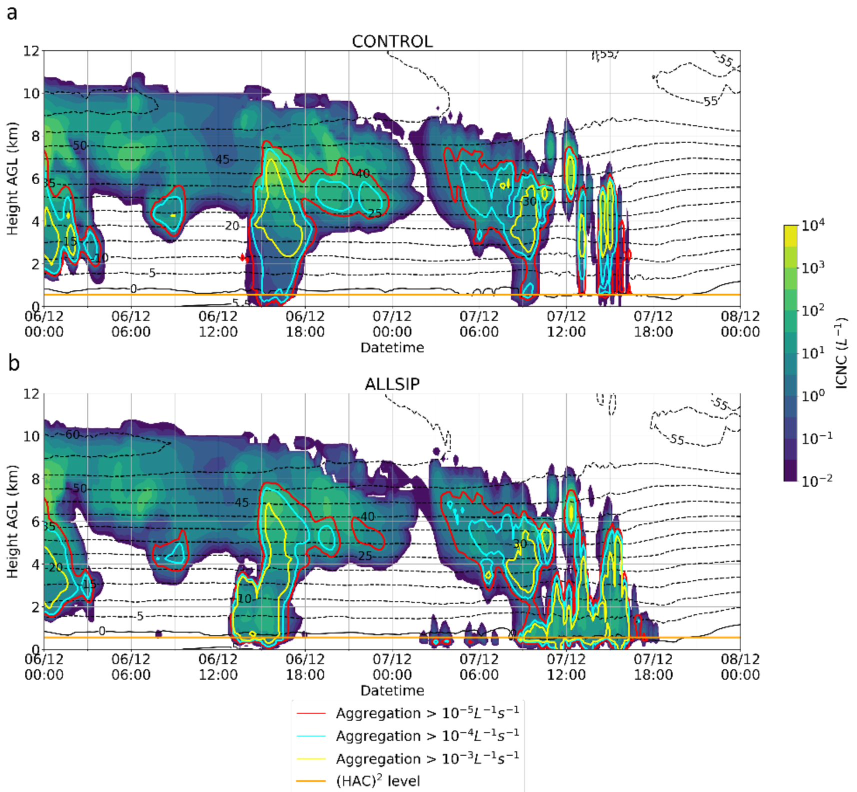

Figure 8: Simulated ICNC (L^{-1}) from the a) CONTROL and b) ALLSIP experiments for SC, with red, cyan, and yellow contours depicting different aggregation rate levels ($L^{-1}s^{-1}$). Black dashed contours indicate temperature in 5°C intervals, and the solid orange line marks the height of the (HAC)^2 station. This time–height cross section is centered over the Achilles Base.

Figure S9 illustrates the temporal evolution of total ice crystal number concentrations (ICNCs) and the relative contributions of the different ice hydrometeor categories. In the CONTROL simulation, pristine ice particles constitute the dominant hydrometeor population, accounting for approximately 20–90% of the total ICNC. Snow contributes between 5% and 40%, with its relative abundance particularly enhanced during 07/12 03–18 UTC. Snow aggregates briefly dominate the ice hydrometeor population during the 2-hour period from 06/12 02–04 UTC; however, total ICNCs remain relatively low during this interval. The total ICNC exhibits three distinct peaks in the CONTROL simulation: approximately 60 L^{-1} at 06/12 00 UTC, 40 L^{-1} at 06/12 15 UTC, and 36 L^{-1} at 07/12 12 UTC, followed by a secondary peak of approximately 20 L^{-1} at 17 UTC. These periods of enhanced ICNC generally coincide with an increased relative contribution from pristine ice particles. In comparison, the ALLSIP simulation generally produces higher total ICNCs, with increases of up to approximately 20%, particularly during the periods of peak concentrations. Pristine ice remains the dominant hydrometeor category throughout much of the period; however, the ALLSIP simulation exhibits a substantially higher peak ICNC of approximately 80 L^{-1}, together with greater temporal variability and generally elevated concentrations. The relative contributions of snow and snow

https://doi.org/10.5194/egusphere-2026-4645
Preprint. Discussion started: 1 September 2026

aggregates are also enhanced, indicating that the inclusion of SIP substantially modifies both the magnitude and composition of the ice hydrometeor population. Graupel and hail generally account for less than 5% of the total ice hydrometeor population in both simulations, except for brief episodes lasting less than one hour, during which their relative contributions can reach approximately 40%. The relative abundance of graupel is enhanced in ALLSIP, suggesting that larger ice particles may also benefit indirectly from SIP through enhanced aggregation with smaller ice particles. In contrast, the relative contribution of hail is reduced in the ALLSIP simulation.

3.6 Comparison of radar signatures: Stratiform Case (SC)

This case also exhibits noteworthy observed features. During the first 24 hours, apart from near-surface clouds, an organized cloud structure spans across 3 and 8 km AGL, with reflectivity values ranging from −30 to +15 dBZ (Fig. 9c). This structure is captured by both the CONTROL (Fig. 9a) and ALLSIP (Fig. 9b) simulations; however, both runs produce excessively high reflectivity (+10 dBZ locally) between 2024-12-06 12 and 18 UTC, indicating intense precipitation not supported by the MIRA observations. During this first 24-hour period, the modeled cloud tops are also overestimated by up to 1 km compared with the observations. The following 24-hour period shows improved agreement, with a well-defined core of high reflectivity (up to 35 dBZ) between 2024-12-07 06 and 18 UTC. As in CC, the ALLSIP simulation yields elevated reflectivity values below 4 km and reproduces the observed spatiotemporal pattern more accurately, suggesting a more realistic representation of hydrometeor growth and sedimentation processes. Similar to CC, time-averaged and maximum reflectivity profiles were calculated over the Achilles Base (Fig. S5b) for the period 7 December 03–21 UTC, encompassing the period of enhanced reflectivity and precipitation. The MIRA time-averaged profile exhibits a pronounced decrease in reflectivity from approximately 15 dBZ near the surface to around 0 dBZ between 1 and 3 km AGL, followed by a gradual decrease with height. CONTROL underestimates the observed mean reflectivity by approximately 1–5 dBZ between 1.5 and 2 km AGL, but overestimates it above approximately 3 km, with differences reaching up to 10 dBZ and averaging around 6 dBZ over the 3–7.5 km AGL layer. In comparison, ALLSIP consistently produces higher mean reflectivity values than CONTROL, by approximately 2 dBZ on average, with the largest difference reaching approximately 7.5 dBZ near 1.5–2 km AGL. Thus, while the activation of SIP processes increases reflectivity in the lower part of the cloud, it also contributes to a larger positive reflectivity bias relative to MIRA in this layer. The maximum reflectivity profiles provide a somewhat different perspective. During the lowest ~2.5 km AGL, ALLSIP produces maximum reflectivity values that are slightly lower than CONTROL, with differences ranging from approximately 0 to −3 dBZ. Above this level, however, ALLSIP produces increasingly higher values, indicating that the activation of SIP processes primarily enhances the strongest simulated hydrometeor signatures at higher levels within the cloud. This vertical redistribution of maximum reflectivity is consistent with the impact of SIP processes on the simulated hydrometeor population and suggests that their inclusion modifies not only the overall reflectivity magnitude but also its vertical distribution. The statistical evaluation of the time-averaged reflectivity profiles provides further context for these differences. Relative to MIRA, CONTROL has a mean bias of 1.97 dBZ, with an MAE and RMSE of 4.84 and 5.50 dBZ, respectively. For ALLSIP, the mean bias is increased to 3.72

https://doi.org/10.5194/egusphere-2026-4645
Preprint. Discussion started: 1 September 2026

dBZ while the MAE and RMSE also increase to 4.87 and 6.14 dBZ, respectively. Therefore, in contrast to the CC case, the inclusion of SIP processes does not lead to an overall reduction in the magnitude of the profile-based errors for this period. Instead, ALLSIP modifies the vertical reflectivity distribution, producing enhanced values in the lower cloud layers and stronger maximum reflectivity signatures aloft, while simultaneously providing a closer qualitative representation of the observed spatiotemporal evolution. These results highlight the case-dependent impact of SIP processes and indicate that their inclusion does not uniformly improve the agreement with observations across all reflectivity metrics. During this period, both simulations capture the observed fluctuations in cloud structure more accurately, with cloud-top heights showing better agreement with the observations. Cloud tops are accurately captured by both CONTROL and ALLSIP during the last 24 h of the simulation. A gradual shift from 8 km to 6.5 km is evident between December 7 03 and 10 UTC, followed by intermittent cloud spikes from 11 to 19 UTC, when cloud tops fluctuate rapidly between 2.5 and 6 km.

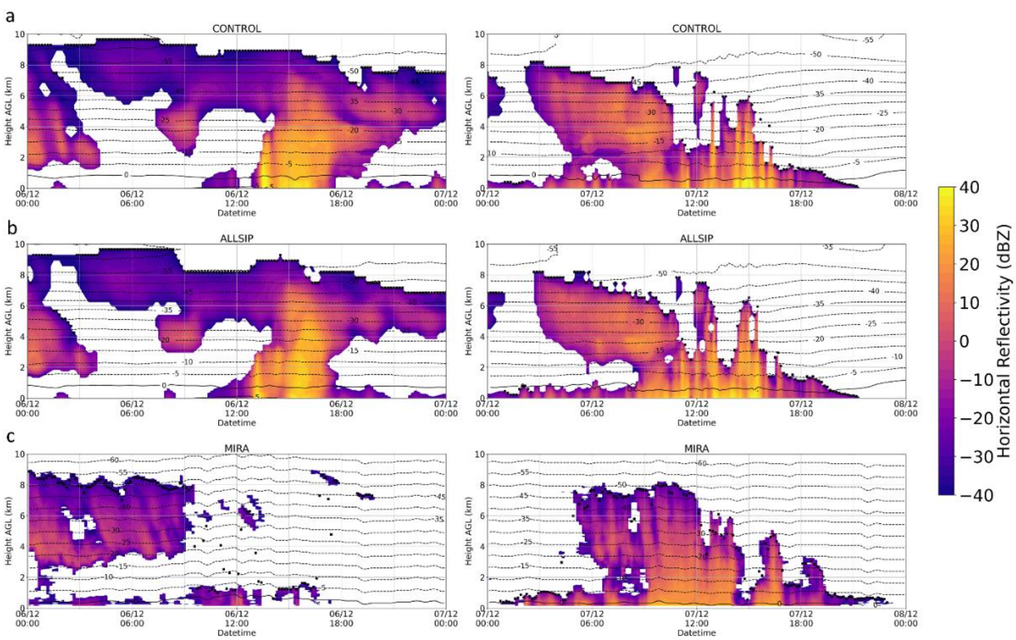

Figure 9: Simulated radar reflectivity (dBz) from CR-SIM, generated using RAMS outputs for the CONTROL (a) and ALLSIP (b) experiments, alongside MIRA in-situ reflectivity observations (c) for SC. Black dashed contours in (a) and (b) represent temperature in 5 °C intervals. Black squares indicate cloud-top height. This time–height cross section is centered over the Achilles Base.

3.7 Spatiotemporal distribution of IWC and LWC - Comparison of IWP and LWP: Stratiform Case (SC)

The spatiotemporal evolution of IWC and LWC is displayed in Fig. S8. In the CONTROL run, the main hydrometeor development occurs on two stages, on December 6 12-18 UTC and December 7 08-18 UTC, with corresponding cloud structure formation. IWC values peak at approximately 1.4 gm^{-3} (December 07, 12-16 UTC), primarily concentrated within the first 2.5 km AGL. Above this level, ice mass is significantly reduced (Fig. S8a). The corresponding LWC field indicates

https://doi.org/10.5194/egusphere-2026-4645
Preprint. Discussion started: 1 September 2026

a rich liquid layer confined mostly below ~1.5 km AGL, with maximum values over 1.8 gm^{-3} occurring around December 7, 12-16 UTC (Fig. S8c).

Similar to CC, the maximum IWC increases to approximately 1.8–2.0 gm^{-3} in the ALLSIP run, with an average increase of 40%, compared to the CONTROL run. The maxima occur with small temporal shifts, within 0.8-2 km AGL, and are also associated with a broader region of elevated ice content. However, in contrast to CC, LWC is significantly reduced in ALLSIP, with peak LWC values reaching ~1.2–1.4 gm^{-3}, opposed to ~1.6–1.8 gm^{-3} in the CONTROL run. The most robust differences between the simulations occur within the ~0.8–2 km AGL layer, corresponding to the mixed-phase temperature regime.

Figure S10 demonstrates the time series of IWP and LWP. During the SC CONTROL run, the IWP is characterized by two outbursts, reaching 1.90 gm^{-2} on December 6, 16 UTC and 3.75 gm^{-2} on December 7, 16 UTC, with smaller secondary peaks around that time (Fig. S10a). The ALLSIP run shows a significant increase of IWP, reaching 3.78 gm^{-2} during the first peak and over 4.00 gm^{-2} during the second peak (Fig. S10a). The average increase throughout the whole period exceeds 40%. These findings highlight the influence of SIP processes. During the same period, the LWP exhibits two pronounced peaks across the same time windows, varying between 0 and 3.55 gm^{-2} (Fig. S10b). The differences between the CONTROL and ALLSIP simulations are profound, with the ALLSIP run showing an average decrease of about 45% during the first peak, and an average increase of up to 50% in the second peak, however there is an average reduction of ~35% for the whole experiment. This amount of reduction is explained by the intense consumption of liquid upon ice growth processes, such as collection, contact freezing, and riming, associated with the increased ice hydrometeors in the ALLSIP scenario.

Focusing on (HAC)^2, observed LWC varies between 0 and 0.35 gm^{-3} on 6 December and between 0.15 and 0.75 gm^{-3} on 7 December (Fig. 10). During the first day, the CONTROL simulation is generally in good agreement with the observations, except for two pronounced peaks at 06/12 14 UTC (0.85 gm^{-3}) and 16 UTC (0.55 gm^{-3}). The corresponding peaks in the ALLSIP simulation are substantially reduced. On 7 December, both CONTROL and ALLSIP showed good agreement with the observations during 00–10 UTC and 18–24 UTC, when observed LWC ranges between approximately 0.25 and 0.75 gm^{-3}. The largest discrepancy occurs during 10–18 UTC. In this period, observations indicate relatively low LWC values, decreasing to approximately 0.15 gm^{-3} between 12 and 14 UTC, whereas both simulations predict a pronounced increase, reaching 1.80 gm^{-3} in CONTROL and 1.45 gm^{-3} in ALLSIP. Nevertheless, ALLSIP consistently produces lower LWC values than CONTROL and is therefore in closer agreement with the observations.

https://doi.org/10.5194/egusphere-2026-4645
Preprint. Discussion started: 1 September 2026

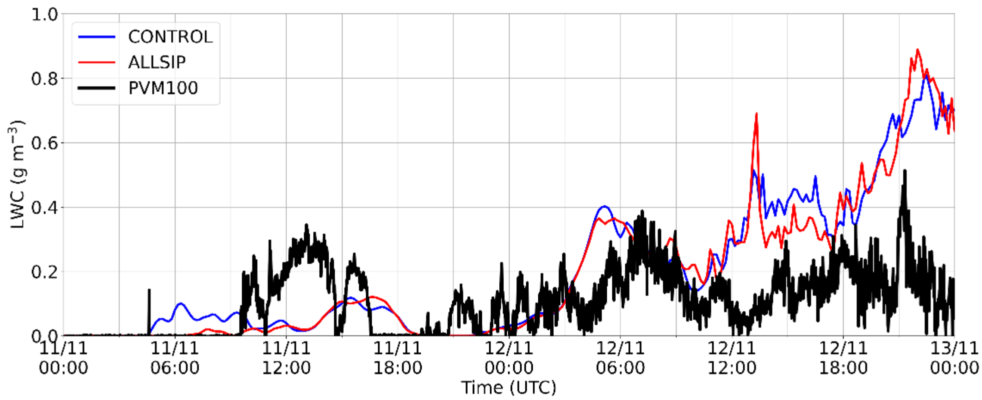

Figure 10: Timeseries of LWC for the stratiform case (SC). The blue line represents the CONTROL, the red line the ALLSIP simulations and the black line observations at (HAC)2 with the PVM-100 instrument.

3.8 Comparison of SIP rates and precipitation: Stratiform Case (SC)

In this experiment (SC), CBR emerges as the dominant SIP mechanism, as displayed in Fig. 11, with two distinct periods of enhanced activity reaching production rates of 10^{-4}-10^{-2} L^{-1}: on 6 December 2024 (12–18 UTC) and 7 December 2024 (10–18 UTC). The second most important mechanism is HM, which also exhibits production rates in the range of 10^{-4}-10^{-2} L^{-1}. The SUBBR process (pink contours) is mainly confined to the −20 to −10°C temperature layer within the lowest ~4 km of the atmosphere and occurs in regions characterized by low ice supersaturation (not shown), consistent with the parameterization of Deshmukh et al. (2022). Mean SUBBR production rates are approximately 10^{-4} L^{-1}. By contrast, the DRS mechanism plays a more limited role in this study. It is activated in the lowest ~2 km of the cloud, at temperatures ranging from −10°C to 3°C (cyan contours). Average production rates for DRS lie between 10^{-6}-10^{-5} L^{-1}. Overall, there is a clear spatial and temporal correspondence between regions of active SIP and enhanced ICNC, although transport and precipitation processes also contribute to shaping the resulting ICNC distributions.

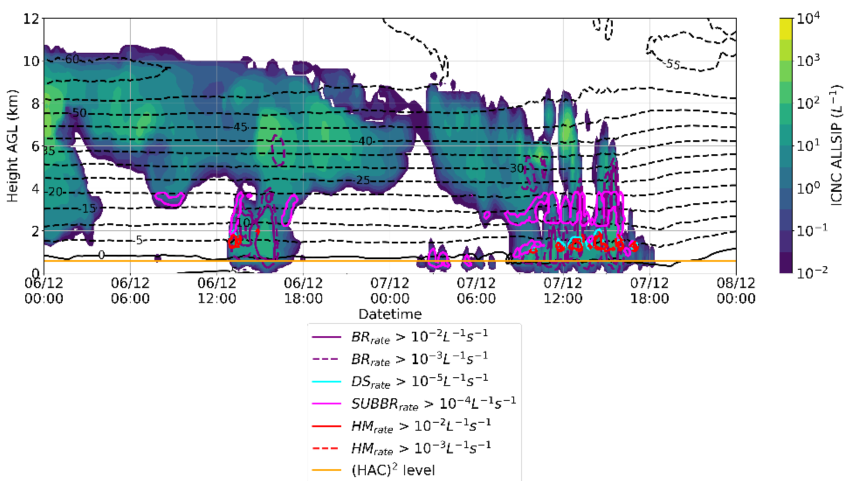

https://doi.org/10.5194/egusphere-2026-4645
Preprint. Discussion started: 1 September 2026

Figure 11: Simulated ICNC (L^{-1}) and SIP production rates from the SC ALLSIP experiments. Solid purple contours indicate areas where $BR_{rate}>10^{-2}$ $L^{-1}s^{-1}$, solid red contours indicate areas where $HM_{rate}>10^{-2}$ $L^{-1}s^{-1}$, dashed red contours areas where $HM_{rate}>10^{-3}$ $L^{-1}s^{-1}$, solid cyan contours areas where $DS_{rate}>10^{-5}$ $L^{-1}s^{-1}$, and solid pink contours areas where $SUBBR_{rate}>10^{-4}$ $L^{-1}s^{-1}$. Black dashed contours indicate temperature in 5°C intervals, and the solid orange line marks the height of the $(HAC)^2$ station. This time–height cross section is centered over the Achilles Base.

Building on the previously discussed spatiotemporal evolution of SIP, we further quantify the relative importance of the individual mechanisms (Fig. 7b). CBR remains the dominant contributor to the total SIP budget, producing 72% of secondary ice. Within this mechanism, snow/aggregate–graupel/hail collisions contribute the most (~37%), followed by snow/aggregate–snow/aggregate (~18%) and cloud ice–snow/aggregate (~18%). Collisions between cloud ice and graupel/hail account for roughly 7%, while interactions involving the largest hydrometeors (graupel or hail) contribute ~3%, with graupel/hail–graupel/hail collisions below 2%. HM is the second-largest source, responsible for ~27% of SIP. SUBBR contributes around 4%, and DS is negligible (<1%). This SIP partition is very similar to CC. Overall, the distribution of SIP mechanisms aligns with prior studies, including Phillips et al. (2017b) and Grzegorczyk et al. (2025a,b), despite variations in cloud dynamics across simulations.

Figure S11 indicates that cumulative precipitation peaks during 06 December (12–16 UTC) and 07 December (09–17 UTC), reaching 78 mm in the CONTROL run versus 66 mm in the experiment (15% reduction). Except for a brief interval on 07 December (12–16 UTC), the CONTROL consistently exceeds the experiment, contrasting with the first experiment and highlighting the nonlinear response of precipitation to SIP. The result is consistent with the studies of Grzegorczyk et al. (2025a,b) and Sun et al. (2025), reflecting the combined influence of cloud dynamics, hydrometeor size distributions, and shifts in the spatiotemporal precipitation pattern.

4 Conclusions

This study presents the successful implementation of three major SIP mechanisms - CBR, DS, SUBBR - within the RAMS-ICLAMS regional modeling system, expanding its capability to represent mixed-phase cloud processes more realistically. The updated model demonstrates substantial improvements in the simulation of ice-phase microphysics, including large increases in ice crystal number concentrations, more accurate vertical cloud structures, and radar reflectivity signatures that show closer agreement with observations from the CHOPIN field campaign. Despite exhibiting broadly similar SIP-induced enhancements in ice water path and hydrometeor aggregation, the two CHOPIN cases - convective and stratiform - responded markedly differently to SIP activation. In the convective case, SIP led to a notable increase in precipitation, whereas the stratiform case experienced a suppression of surface precipitation. These divergent outcomes were accompanied by distinct vertical signatures in radar reflectivity. Furthermore, the spatial distribution of ICNC enhancements differed between the two cases, reflecting case-specific SIP rates and environmental conditions. Collectively, these results demonstrate that SIP processes play a critical role in shaping cloud evolution in alpine environments and that their explicit representation can materially improve the agreement between modeled and observed cloud properties. These results

https://doi.org/10.5194/egusphere-2026-4645
Preprint. Discussion started: 1 September 2026

demonstrate that SIP processes play a critical role in shaping cloud evolution in alpine environments and that their explicit representation can materially improve the agreement between modeled and observed cloud properties.

Several limitations and sources of uncertainty remain. Systematic biases in the simulated radar reflectivity fields point to unresolved uncertainties in particle size distributions, sedimentation rates, and local dynamical processes. The adopted SIP parameterizations also rely on laboratory-derived constants and assumptions, such as fixed rimed fractions and constraints on fragment sizes, which may not fully represent the natural variability of hydrometeor properties in real clouds. In addition, the model resolution does not explicitly resolve fine-scale turbulence, boundary-layer heterogeneity, or microphysical sub-grid variability, while the use of bulk microphysics may introduce further uncertainties in the conditions controlling SIP activation. Finally, the two case studies examined here, although informative, represent only a limited sampling of meteorological regimes and therefore cannot fully characterize the range of SIP impacts across diverse cloud environments.

Nevertheless, the results provide clear evidence that the inclusion of SIP processes leads to a more realistic representation of mixed-phase cloud evolution and precipitation in alpine environments. Importantly, the response to SIP obtained here is consistent with the findings of Georgakaki et al. (2024), who reported similar improvements using the independent WRF-SIP modeling framework. The agreement between two different modeling systems demonstrates that the influence of SIP is not merely a model-specific response but reflects a robust physical signal: explicitly representing SIP substantially alters ice-phase microphysics, cloud structure, and hydrometeor evolution, leading to a better representation of observed atmospheric conditions. The present study provides additional confidence in these findings through the detailed microphysical framework of RAMS-ICLAMS, in which the relevant hydrometeor categories and microphysical processes are explicitly represented. This comprehensive representation provides a well-defined basis for implementing the CBR, DS, and SUBBR mechanisms and offers an advantage over more simplified microphysical approaches with less ice hydrometeor species, by reducing some of the uncertainties associated with representing the interactions among hydrometeors and the resulting SIP processes.

The coherent response of the model to SIP, together with the improvements in ice crystal number concentrations, vertical cloud structure, ice water path, hydrometeor aggregation, and radar reflectivity, demonstrates that the inclusion of these processes leads to a physically meaningful improvement in the simulated atmosphere. While uncertainties in particle properties, sedimentation, sub-grid variability, and SIP parameterizations remain, the overall SIP signal is clear and is consistently supported by the available in-situ and radar observations. In particular, the improved agreement with observations from the CHOPIN field campaign provides strong evidence that incorporating SIP enables the model to better capture the complex evolution of mixed-phase clouds and, more broadly, to provide a more realistic description of atmospheric conditions in alpine environments.

These findings highlight the importance of explicitly accounting for SIP in regional atmospheric modeling and provide further support for considering SIP processes when simulating cloud systems in complex orographic environments. Future work should extend the validation to a broader range of synoptic conditions, seasons, and geographic regions to better constrain the behavior and importance of SIP across different cloud regimes. Such efforts should combine high-resolution simulations with polarimetric radar observations, in-situ microphysical measurements, data assimilation techniques, and improved representations of turbulence and microphysical sub-grid variability. In particular, turbulence parameterizations that account for the anisotropic nature of flow in orographic regions may further improve the representation of the environmental conditions controlling SIP activation. Ultimately, the consistent SIP response obtained across independent modeling frameworks, together with the added value of the detailed microphysical process representation in RAMS-ICLAMS, supports the further development and implementation of SIP parameterizations in operational forecasting and climate-scale modeling systems. This will be essential for improving the prediction of precipitation and cloud properties and for better quantifying the role of mixed-phase clouds in cloud-radiative interactions and long-term climate projections.

Code and data availability

The data from the meteorological radar data is available at: https://doi.org/10.5281/zenodo.21245825. All associated observational datasets, RAMS-ICLAMS model outputs, and Python scripts for reproducing the manuscript figures are archived and publicly available at: https://doi.org/10.5281/zenodo.21837262.

Supplement link

The link to the supplement will be included by Copernicus, if applicable.

Author contributions

IC: Conceptualization, methodology, investigation, model development, model simulations, formal analysis, statistical assessment of the results, analysis of observational datasets, and writing - original draft.
PG: Supervision and guidance on model development, overview of the numerical simulation, contribution to writing and editing of the original draft.
MGi and AP: Contribution to the observational dataset analysis
RF: Provision and analysis of DMT CCN-100 and PINE data.
MGn and KE: Provision and analysis of meteorological observations from the (HAC)2 observatory and contribution to the observational dataset analysis and provision of PVM-100 observations.
PP: Supervision and scientific guidance on model development, drawing on their expertise with the RAMS-ICLAMS modeling framework, and contribution to writing—review and editing.
NC and AB: Analysis and provision of MIRA cloud radar observations and contribution to the comparison of observational and simulated radar fields.
HF and EB: Scientific guidance and overview of the work and contribution to writing - review and editing.

AN: Conceptualization and design of the study, design and overview of the CHOPIN campaign, scientific guidance, and contribution to writing - review and editing.

All authors contributed to discussions of the manuscript and reviewed and commented on the manuscript.

Competing interests

The contact author has declared that neither they nor their co-authors have any competing interests.

Disclaimer

Copernicus Publications adds a standard disclaimer: "Copernicus Publications remains neutral with regard to jurisdictional claims made in the text, published maps, institutional affiliations, or any other geographical representation in this paper. While Copernicus Publications makes every effort to include appropriate place names, the final responsibility lies with the authors. Views expressed in the text are those of the authors and do not necessarily reflect the views of the publisher."

Please feel free to add disclaimer text at your choice, if applicable.

Acknowledgements

We acknowledge support from the Horizon Europe CleanCloud project, no. 101137639.

Financial support

PG acknowledges a personal PostDoc mobility grant from the Swiss National Science Foundation (grant no. 225474).

Review statement

The review statement will be added by Copernicus Publications listing the handling editor as well as all contributing referees according to their status anonymous or identified.

References

Calderón, S. M., Hyttinen, N., Kokkola, H., Raatikainen, T., Lawson, R. P., and Romakkaniemi, S.: Secondary ice formation in cumulus congestus clouds: insights from observations and aerosol-aware large-eddy simulations, Atmos. Chem. Phys., 25, 14479–14500, https://doi.org/10.5194/acp-25-14479-2025, 2025

https://doi.org/10.5194/egusphere-2026-4645
Preprint. Discussion started: 1 September 2026

Costa-Surós, M., Gonçalves Ageitos, M., Chatziparaschos, M., Georgakaki, P., Thomas, M. A., Montané Pinto, G., Myriokefalitakis, S., van Noije, T., Le Sager, P., Kanakidou, M., Nenes, A., and Pérez García-Pando, C.: Implementation of primary and secondary ice production in EC-Earth3-AerChem: global impacts and insights, Atmos. Chem. Phys., 26, 2667–2690, https://doi.org/10.5194/acp-26-2667-2026, 2026

Cotton, W. R., Tripoli, G. J., Rauber, R. M., and Mulvihill, E. A.: Numerical Simulation of the Effects of Varying Ice Crystal Nucleation Rates and Aggregation Processes on Orographic Snowfall, J. Clim. Appl. Meteor., 25, 1658–1680, https://www.jstor.org/stable/26183490, 1986

Cotton, W. R., Pielke Sr., R. A., Walko, R. L., Liston, G. E., Tremback, C. J., Jiang, H., McAnelly, R. L., Harrington, J. Y., Nicholls, M. E., Carrio, G. G., and McFadden, J. P.: RAMS 2001: Current status and future directions, Meteor. Atmos. Physics, 82, 5–29, https://doi.org/10.1007/s00703-001-0584-9, 2003

Crosier, J., Bower, K. N., Choularton, T. W., Westbrook, C. D., Connolly, P. J., Cui, Z. Q., Crawford, I. P., Capes, G. L., Coe, H., Dorsey, J. R., Williams, P. I., Illingworth, A. J., Gallagher, M. W., and Blyth, A. M.: Observations of ice multiplication in a weakly convective cell embedded in supercooled mid-level stratus, Atmos. Chem. Phys., 11, 257–273, https://doi.org/10.5194/acp-11-257-2011, 2011

Dedekind, Z., Proske, U., Ferrachat, S., Lohmann, U., and Neubauer, D.: Simulating the seeder–feeder impacts on cloud ice and precipitation over the Alps, Atmos. Chem. Phys., 24, 5389–5404, https://doi.org/10.5194/acp-24-5389-2024, 2024.

DeMott, P. J., Prenni, A. J., Liu, X., Kreidenweis, S. M., Petters, M. D., Twohy, C. H., Richardson, M. S., Eidhammer, T., and Rogers, D. C.: Predicting global atmospheric ice nuclei distributions and their impacts on climate, P. Natl. Acad. Sci. USA, 107, 11217–11222, https://doi.org/10.1073/pnas.0910818107, 2010

Deshmukh, A., Phillips, V. T. J., Bansemer, A., Patade, S., and Waman, D.: New Empirical Formulation for the Sublimational Breakup of Graupel and Dendritic Snow, J. Atmos. Sci., 79, 317–336, https://doi.org/10.1175/JAS-D-20-0275.1, 2022

Dong, Y. Y., Oraltay, R. G., and Hallett, J.: Ice particle generation during evaporation, Atmos. Res., 32, 45–53, https://doi.org/10.1016/0169-8095(94)90050-7, 1994

Feingold, G., Walko, R. L., Stevens, B., and Cotton, W. R.: Simulations of marine stratocumulus using a new microphysical parameterization scheme, Atmos. Res., 47–48, 505–528, https://doi.org/10.1016/S0169-8095(98)00058-1, 1998

Ferrier, B. S.: A Double-Moment Multiple-Phase Four-Class Bulk Ice Scheme. Part I: Description, J. Atmos. Sci., 51, 249–280, https://doi.org/10.1175/1520-0469(1994)051<0249:ADMMPF>2.0.CO;2, 1994.

Field, P. R., Möhler, O., Connolly, P., Krämer, M., Cotton, R., Heymsfield, A. J., Saathoff, H., and Schnaiter, M.: Some ice nucleation characteristics of Asian and Saharan desert dust, Atmos. Chem. Phys., 6, 2991–3006, https://doi.org/10.5194/acp-6-2991-2006, 2006.

Field, P. R., Lawson, R. P., Brown, P. R. A., Lloyd, G., Westbrook, C., Moisseev, D., Miltenberger, A., Nenes, A., Blyth, A., Choularton, T., Connolly, P., Buehl, J., Crosier, J., Cui, Z., DeMott, P., Flossmann, A., Heymsfield, A., Huang, Y., Kalesse, H., Kanji, Z. A., Korolev, A., Kirchgaessner, A., Lasher-Trapp, S., Leisner, T., McFarquhar, G., Phillips, V., Stith, J., and Sullivan, S.: Secondary ice production: Current state of the science and recommendations for the future, Meteorol. Monogr., 58, 7.1–7.20, https://doi.org/10.1175/AMSMONOGRAPHS-D-16-0014.1, 2017

Floka, F., Patlakas, P., Chaniotis, I., Georgakaki, P., Flocas, H., Nenes, A., and Sotiropoulou, G.: Ice multiplication modulates the medicane's track and thermodynamic evolution, Geophys. Res. Lett., 53, e2025GL120145, https://doi.org/10.1029/2025GL120145, 2026

Fountoukis, C. and Nenes, A.: Continued development of a cloud droplet formation parameterization for global climate models, J. Geophys. Res., 110, D11212, https://doi.org/10.1029/2004JD005591, 2005.

Frostenberg, H. C., Costa-Surós, M., Georgakaki, P., Proske, U., Sotiropoulou, G., May, E., Neubauer, D., Eriksson, P., Ageitos, M.G., Nenes, A., García-Pando, C.P., Seland, Ø., and Ickes, L.: Large discrepancies in dominant microphysical processes governing mixed-phase clouds across climate models, npj Clim. Atmos. Sci., 9, https://doi.org/10.1038/s41612-026-01342-7, 2026.

Galani, E., D. Balis, P. Zanis, C. Zerefos, A. Papayannis, H. Wernli, and E. Gerasopoulos, Observations of stratosphere-troposphere transport events over the eastern Mediterranean using a ground-based lidar system, J. Geophys. Res., 108(D12), 8527, doi:10.1029/2002JD002596, 2003.

Gautam, M., Phillips, V. T. J., Patade, S., Bansemer, A., Waman, D., and Heymsfield, A. J.: Fragmentation in Collisions of Snow with Graupel/Hail: New Formulation from Field Observations, J. Atmos. Sci., 81, 2149–2164, https://doi.org/10.1175/JAS-D-23-0122.1, 2024.

Georgakaki, P., Sotiropoulou, G., Vignon, É., Billault-Roux, A.-C., Berne, A., and Nenes, A.: Secondary ice production processes in wintertime alpine mixed-phase clouds, Atmos. Chem. Phys., 22, 1965–1988, https://doi.org/10.5194/acp-22-1965-2022, 2022.

Georgakaki, P., Billault-Roux, A.-C., Foskinis, R., Gao, K., Sotiropoulou, G., Gini, M., Takahama, S., Eleftheriadis K., Papayannis, A., Berne, A., and Nenes, A.: Unraveling ice multiplication in winter orographic clouds via in-situ observations, remote sensing and modeling, npj Clim. Atmos. Sci., 7, 145, https://doi.org/10.1038/s41612-024-00671-9, 2024.

Grzegorczyk, P., Yadav, S., Zanger, F., Theis, A., Mitra, S. K., Borrmann, S., and Szakáll, M.: Fragmentation of ice particles: laboratory experiments on graupel–graupel and graupel–snowflake collisions, Atmos. Chem. Phys., 23, 13505–13521, https://doi.org/10.5194/acp-23-13505-2023, 2023

Grzegorczyk, P., Wobrock, W., Dziduch, A., and Planche, C.: Influence of secondary ice production on cloud and rain properties: analysis of the HYMEX IOP7a heavy-precipitation event, Atmos. Chem. Phys., 25, 10403–10420, https://doi.org/10.5194/acp-25-10403-2025, 2025.

Grzegorczyk, P., Wobrock, W., Canzi, A., Niquet, L., Tridon, F., and Planche, C.: Investigating secondary ice production in a deep convective cloud with a 3D bin microphysics model: Part II -Effects on the cloud formation and development, Atmos. Res., 314, 107797, https://doi.org/10.1016/j.atmosres.2024.107797, 2025.

https://doi.org/10.5194/egusphere-2026-4645
Preprint. Discussion started: 1 September 2026

Hallett, J. and Mossop, S. C.: Production of secondary ice particles during the riming process, Nature, 249, 26–28, https://doi.org/10.1038/249026a0, 1974.

Harrington, J. Y.: The effects of radiative and microphysical processes on simulated warm and transition season Arctic stratus, PhD Diss., Atmospheric Science Paper No. 637, Colorado State University, Fort Collins, CO, 1997.

Hersbach, H., Bell, B., Berrisford, P., et al.: The ERA5 global reanalysis, Q. J. R. Meteorol. Soc., 146, 1999–2049, https://doi.org/10.1002/qj.3803, 2020.

Heymsfield, A. J. and Mossop, S. C.: Temperature dependence of secondary ice crystal production during soft hail growth by riming, Q. J. R. Meteor. Soc., 110, 765–770, https://doi.org/10.1002/qj.49711046512, 1984.

Heymsfield, A. J., Schmitt, C., Chen, C.-C. J., Bansemer, A., Gettelman, A., and D. R. S.: Contributions of the Liquid and Ice Phases to Global Surface Precipitation: Observations and Global Climate Modeling, J. Atmos. Sci., 77, 2629–2648, https://doi.org/10.1175/JAS-D-19-0352.1, 2020.

Hoarau, T., Pinty, J.-P., and Barthe, C.: A representation of the collisional ice break-up process in the two-moment microphysics LIMA v1.0 scheme of Meso-NH, Geosci. Model Dev., 11, 4269–4289, https://doi.org/10.5194/gmd-11-4269-2018, 2018.

Huang, Y., Wu, W., Gao, W., Fu, Y., and He, J.: Microphysical processes producing high ice water contents (HIWCs) in tropical convective clouds during the HAIC-HIWC field campaign: Dominant role of secondary ice production, Atmos. Chem. Phys., 22, 2365–2384, https://doi.org/10.5194/acp-22-2365-2022, 2022.

James, R. L., Phillips, V. T. J., and Connolly, P. J.: Secondary ice production during the break-up of freezing water drops on impact with ice particles, Atmos. Chem. Phys., 21, 18519–18530, https://doi.org/10.5194/acp-21-18519-2021, 2021.

Kain, J. S. and Fritsch, J. M.: Convective Parameterization for Mesoscale Models: The Kain-Fritsch Scheme, in: The Representation of Cumulus Convection in Numerical Models, edited by: Emanuel, K. A. and Raymond, D. J., Meteorological Monographs, American Meteorological Society, Boston, MA, https://doi.org/10.1007/978-1-935704-13-3_16, 1993.

Korolev, A. and Field, P. R.: The Effect of Dynamics on Mixed-Phase Clouds: Theoretical Considerations, J. Atmos. Sci., 65, 66–86, https://doi.org/10.1175/2007JAS2355.1, 2008.

Korolev, A. and Leisner, T.: Review of experimental studies of secondary ice production, Atmos. Chem. Phys., 20, 11767–11797, https://doi.org/10.5194/acp-20-11767-2020, 2020.

Korolev, A., DeMott, P. J., Heckman, I., Wolde, M., Williams, E., Smalley, D. J., and Donovan, M. F.: Observation of secondary ice production in clouds at low temperatures, Atmos. Chem. Phys., 22, 13103–13113, https://doi.org/10.5194/acp-22-13103-2022, 2022.

Meyers, M. P., DeMott, P. J., and Cotton, W. R.: New Primary Ice-Nucleation Parameterizations in an Explicit Cloud Model, J. Appl. Meteor. Climatol., 31, 708–721, https://doi.org/10.1175/1520-0450(1992)031<0708:NPINPI>2.0.CO;2, 1992.

https://doi.org/10.5194/egusphere-2026-4645
Preprint. Discussion started: 1 September 2026

Meyers, M. P., Walko, R. L., Harrington, J. Y., and Cotton, W. R.: New RAMS cloud microphysics parameterization. Part II: The two-moment scheme, Atmos. Res., 45, 3–39, https://doi.org/10.1016/S0169-8095(97)00018-5, 1997.

Milbrandt, J. A. and Yau, M. K.: A Multimoment Bulk Microphysics Parameterization. Part I: Analysis of the Role of the Spectral Shape Parameter, J. Atmos. Sci., 62, 3051–3064, https://doi.org/10.1175/JAS3534.1, 2005.

Milbrandt, J. A. and Yau, M. K.: A Multimoment Bulk Microphysics Parameterization. Part II: A Proposed Three-Moment Closure and Scheme Description, J. Atmos. Sci., 62, 3065–3081, https://doi.org/10.1175/JAS3535.1, 2005.

Möhler, O., Adams, M., Lacher, L., Vogel, F., Nadolny, J., Ullrich, R., Boffo, C., Pfeuffer, T., Hobl, A., Weiß, M., Vepuri, H. S. K., Hiranuma, N., and Murray, B. J.: The Portable Ice Nucleation Experiment (PINE): a new online instrument for laboratory studies and automated long-term field observations of ice-nucleating particles, Atmos. Meas. Tech., 14, 1143–1166, https://doi.org/10.5194/amt-14-1143-2021, 2021.

Mülmenstädt, J., Sourdeval, O., Delanoë, J., and Quaas, J.: Frequency of occurrence of rain from liquid-, mixed-, and ice-phase clouds derived from A-Train satellite retrievals, Geophys. Res. Lett., 42, 6502–6509, https://doi.org/10.1002/2015GL064604, 2015.

Nenes, A. and Seinfeld, J. H.: Parameterization of cloud droplet formation in global climate models, J. Geophys. Res., 108, 4415, https://doi.org/10.1029/2002JD002911, 2003.

Oue, M., Tatarevic, A., Kollias, P., Wang, D., Yu, K., and Vogelmann, A. M.: The Cloud-resolving model Radar SIMulator (CR-SIM) Version 3.3: description and applications of a virtual observatory, Geosci. Model Dev., 13, 1975–1998, https://doi.org/10.5194/gmd-13-1975-2020, 2020.

Papayannis, A. D., Gidarakou, M., Kafenidis, N., Veselovskii, I., Foskinis, R., Zografou, O., Gini, M. I., Granakis, K., Zieger, P., Jonsson, A., Schmale, J., Eleftheriadis, K., and Nenes, A.: Vertical profiling of aerosol optical, microphysical, and chemical properties using elastic-Raman-LIF lidars and in situ aerosol measurements during the 2024–2025 CHOPIN campaign, EGU General Assembly 2026, Vienna, Austria, 3–8 May 2026, EGU26-14184, https://doi.org/10.5194/egusphere-egu26-14184, 2026

Phillips, V. T. J., Yano, J., and Khain, A.: Ice Multiplication by Breakup in Ice–Ice Collisions. Part I: Theoretical Formulation, J. Atmos. Sci., 74, 1705–1719, https://doi.org/10.1175/JAS-D-16-0224.1, 2017.

Phillips, V. T. J., Yano, J., Khain, A., and Benmoshe, N.: Ice Multiplication by Breakup in Ice–Ice Collisions. Part II: Numerical Simulations, J. Atmos. Sci., 74, 2789–2811, https://doi.org/10.1175/JAS-D-16-0223.1, 2017.

Phillips, V. T. J., Patade, S., Gutierrez, J., and Bansemer, A.: Secondary Ice Production by Fragmentation of Freezing Drops: Formulation and Theory, J. Atmos. Sci., 75, 3031–3070, https://doi.org/10.1175/JAS-D-17-0190.1, 2018.

Pielke, R. A., Cotton, W. R., Walko, R. L., Tremback, C. J., Lyons, W. A., Grasso, L. D., Nicholls, M. E., Moran, M. D., Wesley, D. A., Lee, T. J., and Copeland, J. H.: A comprehensive meteorological modeling system – RAMS, Meteorol. Atmos. Phys., 49, 69–91, https://doi.org/10.1007/BF01025401, 1992.

https://doi.org/10.5194/egusphere-2026-4645
Preprint. Discussion started: 1 September 2026

Proske, U., Bessenbacher, V., Dedekind, Z., Lohmann, U., and Neubauer, D.: How frequent is natural cloud seeding from ice cloud layers (< −35 °C) over Switzerland?, Atmos. Chem. Phys., 21, 5195–5216, https://doi.org/10.5194/acp-21-5195-2021, 2021.

Pruppacher, H. R. and Klett, J. D.: Microphysics of Clouds and Precipitation, Kluwer Academic, 954 pp., 1997.

Qu, Y., Khain, A., Phillips, V., Ilotoviz, E., Shpund, J., Patade, S., and Chen, B.: The role of ice splintering on microphysics of deep convective clouds forming under different aerosol conditions: Simulations using the model with spectral bin microphysics, J. Geophys. Res. Atmos., 125, e2019JD031312, https://doi.org/10.1029/2019JD031312, 2020.

Qu, Z., Korolev, A., Milbrandt, J. A., Heckman, I., Cholette, M., Nguyen, C., and Wolde, M.: The impacts of secondary ice production on the microphysics and dynamics of mid-latitude cold season convection, Atmos. Chem. Phys., 25, 17845–17868, https://doi.org/10.5194/acp-25-17845-2025, 2025

Roberts, G. C. and Nenes, A.: A Continuous-Flow Streamwise Thermal-Gradient CCN Chamber for Atmospheric Measurements, Aerosol Sci. Tech., 39, 206–221, https://doi.org/10.1080/027868290913988, 2005.

Saleeby, S. M. and Cotton, W. R.: A Large-Droplet Mode and Prognostic Number Concentration of Cloud Droplets in the Colorado State University Regional Atmospheric Modeling System (RAMS). Part I: Module Descriptions and Supercell Test Simulations, J. Appl. Meteor. Climatol., 43, 182–195, https://doi.org/10.1175/1520-0450(2004)043<0182:ALMAPN>2.0.CO;2, 2004

Saleeby, S. M. and Cotton, W. R.: A Binned Approach to Cloud-Droplet Riming Implemented in a Bulk Microphysics Model, J. Appl. Meteor. Climatol., 47, 694–703, https://doi.org/10.1175/2007JAMC1664.1, 2008

Saleeby, S. M. and van den Heever, S. C.: Developments in the CSU-RAMS Aerosol Model: Emissions, Nucleation, Regeneration, Deposition, and Radiation, J. Appl. Meteor. Climatol., 52, 2601–2622, https://doi.org/10.1175/JAMC-D-12-0312.1, 2013.

Solomos, S., Kallos, G., Kushta, J., Astitha, M., Tremback, C., Nenes, A., and Levin, Z.: An integrated modeling study on the effects of mineral dust and sea salt particles on clouds and precipitation, Atmos. Chem. Phys., 11, 873–892, https://doi.org/10.5194/acp-11-873-2011, 2011.

Sotiropoulou, G., Sullivan, S., Savre, J., Lloyd, G., Lachlan-Cope, T., Ekman, A. M. L., and Nenes, A.: The impact of secondary ice production on Arctic stratocumulus, Atmos. Chem. Phys., 20, 1301–1316, https://doi.org/10.5194/acp-20-1301-2020, 2020.

Sotiropoulou, G., Vignon, É., Young, G., Morrison, H., O'Shea, S. J., Lachlan-Cope, T., Berne, A., and Nenes, A.: Secondary ice production in summer clouds over the Antarctic coast: an underappreciated process in atmospheric models, Atmos. Chem. Phys., 21, 755–771, https://doi.org/10.5194/acp-21-755-2021, 2021.

Spyrou, C., Mitsakou, C., Kallos, G., Louka, P., and Vlastou, G.: An improved limited area model for describing the dust cycle in the atmosphere, J. Geophys. Res., 115, D17211, https://doi.org/10.1029/2009JD013682, 2010.

Storelvmo, T.: Aerosol Effects on Climate via Mixed-Phase and Ice Clouds, Annu. Rev. Earth Planet. Sci., 45, 199–222, https://doi.org/10.1146/annurev-earth-060115-012240, 2017.

Sun, M., Connolly, P. J., Field, P. R., Finney, D. L., and Blyth, A. M.: Influence of secondary ice formation on tropical deep convective clouds simulated by the Unified Model, Atmos. Chem. Phys., 25, 18549–18569, https://doi.org/10.5194/acp-25-18549-2025, 2025.

Takahashi, T., Nagao, Y., and Kushiyama, Y.: Possible high ice particle production during graupel-graupel collisions, J. Atmos. Sci., 52, 4523–4527, https://doi.org/10.1175/1520-0469(1995)052<4523:PHIPPD>2.0.CO;2, 1995.

Tan, I. and Storelvmo, T.: Evidence of Strong Contributions From Mixed-Phase Clouds to Arctic Climate Change, Geophys. Res. Lett., 46, 2894–2902, https://doi.org/10.1029/2018GL081871, 2019.

Tzivion, S., Feingold, G., and Levin, Z.: An Efficient Numerical Solution to the Stochastic Collection Equation, J. Atmos. Sci., 44, 3139–3149, https://doi.org/10.1175/1520-0469(1987)044<3139:AENSTT>2.0.CO;2, 1987

Vardiman, L.: The Generation of Secondary Ice Particles in Clouds by Crystal–Crystal Collision, J. Atmos. Sci., 35, 2168–2180, https://doi.org/10.1175/1520-0469(1978)035<2168:TGOSIP>2.0.CO;2, 1978.

Vergara-Temprado, J., Miltenberger, A. K., Furtado, K., Grosvenor, D. P., Shipway, B. J., Hill, A. A., Wilkinson, J. M., Field, P. R., Murray, B. J., and Carslaw, K. S.: Strong control of Southern Ocean cloud reflectivity by ice-nucleating particles, P. Natl. Acad. Sci. USA, 115, 2687–2692, https://doi.org/10.1073/pnas.1721627115, 2018.

Vignon, É., Besic, N., Jullien, N., Gehring, J., and Berne, A.: Microphysics of Snowfall Over Coastal East Antarctica Simulated by Polar WRF and Observed by Radar, J. Geophys. Res. Atmos., 124, 11452–11476, https://doi.org/10.1029/2019JD031028, 2019

Vignon, É., Alexander, S. P., DeMott, P. J., Sotiropoulou, G., Gerber, F., Hill, T. C. J., et al. (2021). Challenging and improving the simulation of mid-level mixed-phase clouds over the high-latitude Southern Ocean. Journal of Geophysical Research: Atmospheres, 126, e2020JD033490. https://doi.org/10.1029/2020JD033490

Walko, R. L., Cotton, W. R., Meyers, M. P., and Harrington, J. Y.: New RAMS cloud microphysics parameterization. Part I: The single moment scheme, Atmos. Res., 38, 29–62, https://doi.org/10.1016/0169-8095(94)00087-T, 1995.

Walko, R. L., Cotton, W. R., Feingold, G., and Stevens, B.: Efficient computation of vapor and heat diffusion between hydrometeors in a numerical model, Atmos. Res., 53, 171–183, https://doi.org/10.1016/S0169-8095(99)00044-7, 2000.

Waman, D., Meusel, J., Keshtgar, B., Wallentin, G., Barthlott, C., Patade, S., Shete, S., Prabhakaran, T., Fievet, R., Finney, D., Blyth, A., and Hoose, C.: Impacts of Secondary Ice Production on the Microphysics and Dynamics of Deep Convective Clouds in Different Environments, EGUsphere [preprint], https://doi.org/10.5194/egusphere-2025-6129, 2026

Zhao, X., Liu, X., Phillips, V. T. J., and Patade, S.: Impacts of secondary ice production on Arctic mixed-phase clouds based on ARM observations and CAM6 single-column model simulations, Atmos. Chem. Phys., 21, 5685–5703, https://doi.org/10.5194/acp-21-5685-2021, 2021.